

Impacts of Lower Thermospheric Atomic Oxygen and Dynamics on the Thermospheric Semiannual Oscillation using GITM and WACCM-X

Garima Malhotra ^{1,2}, Aaron J. Ridley ¹, McArthur Jones Jr. ³

¹Climate and Space Sciences and Engineering, University of Michigan, Ann Arbor, Michigan, USA.

²CIRES, University of Colorado, Boulder, Colorado, USA.

³Space Science Division, U.S. Naval Research Laboratory, Washington, DC, USA.

Key Points:

- Atomic oxygen in MLT from SABER and WACCM-X has an SAO with maxima at solstices and at summer mid-high latitudes, opposite to that of MSIS.
- GITM reproduces the T-I SAO with equinoctial maxima using MSIS [O] at lower boundary and with solstitial maxima using WACCM-X [O].
- GITM does not change the SAO phase between MLT and upper thermosphere on a seasonal scale.

Corresponding author: Garima Malhotra, garimam@umich.edu

This is the author manuscript accepted for publication and has undergone full peer review but has not been through the copyediting, typesetting, pagination and proofreading process, which may lead to differences between this version and the [Version of Record](#). Please cite this article as [doi: 10.1029/2021JA029320](https://doi.org/10.1029/2021JA029320).

This article is protected by copyright. All rights reserved.

Abstract

The latitudinal and temporal variation of atomic oxygen (O) is opposite between the empirical model, NRLMSISE-00 (MSIS) and the whole atmosphere model, WACCM-X at 97-100 km. Atomic Oxygen from WACCM-X has maxima at solstices and summer mid-high latitudes, similar to [O] from SABER. We use the densities and dynamics from WACCM-X to drive the Global Ionosphere Thermosphere Model (GITM) at its lower boundary, and compare it with the MSIS driven GITM. We focus on the differences in the modeling of the thermospheric and ionospheric semiannual oscillation (T-I SAO). Our results reveal that driving GITM with WACCM-X causes the T-I SAO to maximize around solstices, opposite to when MSIS is used. This is because the global mixing in GITM during solstices is not strong enough to decrease the solstitial [O] densities below the equinoctial values between MLT and upper thermosphere. Larger summer [O] in the MLT leads to the accumulation of [O] at lower latitudes in the thermosphere due to weaker meridional transport, which further increases the amplitude of the oppositely-phased SAO. WACCM-X itself has the right phase of SAO in the upper thermosphere but wrong at lower altitudes. The exact mechanisms that can correct the phase of T-I SAO in GITM while using SABER-like [O] in the MLT are currently unknown and warrant further investigation. We suggest mechanisms that can reduce the solstitial maxima in the lower thermosphere, for example, stronger interhemispheric meridional winds, stronger residual circulation, seasonal variations in eddy diffusion, and momentum from breaking gravity waves.

1 Introduction

The Earth's atmosphere is an open system with complex interplay between internal and external drivers resulting in complicated non-linear coupling mechanisms. The region above 100 km is usually referred to as the Earth's upper atmosphere with the neutral thermosphere coexisting with the partly ionized ionosphere. Both the thermosphere and ionosphere exhibit several periodic variations in densities and temperature across an array of time scales ranging from minutes to a few years (Rishbeth, 2007). These include variations due to gravity waves (e.g., S. L. Bruinsma & Forbes, 2008; Miyoshi et al., 2014), tides (e.g., Forbes et al., 2009; Hagan et al., 2009), planetary waves (Sassi et al., 2016), annual and semiannual oscillation (e.g. Jones Jr., Emmert, et al., 2018), quasi-biennial oscillation (e.g. Malhotra et al., 2016), and 11-year solar cycle (e.g., J. T. Emmert et al., 2008; Burns et al., 2015). Amongst the long term variations, the thermospheric and ionospheric annual oscillation (T-I AO) and the semiannual oscillation (T-I SAO) have the largest magnitudes and were initially observed in neutral densities derived from satellite drag measurements by Paetzold and Zschörner (1961). The global T-I AO has a minimum in neutral densities in July and has partially been attributed to the changing distance between the Sun and the Earth (Volland et al., 1972), and is still under investigation (e.g. Qian et al., 2009). In this study, we mainly focus on the T-I SAO. We will briefly review some of the pioneering works on T-I SAO in the following section.

1.1 Previous Work

The global T-I SAO has maxima in April and October and minima in January and July, and was initially hypothesized to be driven by the semiannual effect of geomagnetic activity (Paetzold & Zschörner, 1961). However, the SAO in geomagnetic activity itself was not well understood at the time (e.g., Bartels, 1932; Boller & Stolov, 1970). Amongst many theories, the Russell-McPherron (R-M) effect (C. T. Russell & McPherron, 1973) has been studied widely to explain the semiannual variation in geomagnetic activity. In this mechanism, during equinoxes, the magnetic field of the Sun in the ecliptic plane has larger southward magnitude at Earth in the Geocentric Solar Magnetospheric (GSM) coordinates, resulting in stronger reconnection events. Walterscheid (1982) suggested that the semiannual variation in temperature (Joule Heating) due to R-M effect is responsible for the globally averaged SAO in mass density. After Paetzold and Zschörner (1961),

66 several other studies observed the SAO signature in O/N₂, atomic oxygen (O), temper-
67 ature and the ionospheric F2 layer (e.g., King-Hele, 1966, 1967; King-Hele & Kingston,
68 1968; Jacchia et al., 1969; T. J. Fuller-Rowell, 1998; Rishbeth et al., 2000; Rishbeth &
69 Mendillo, 2001). The amplitude of the global T-I SAO has been recorded to be ~15%
70 in mass density at 400 km and ionospheric Total Electron Content (TEC) relative to the
71 global annual average (J. Emmert, 2015; Jones Jr. et al., 2017). The T-I SAO was ini-
72 tially reproduced using temperature variations by the Jacchia series of thermospheric mod-
73 els (Jacchia, 1965, 1970). However, it was later observed that the temperature variations
74 could not completely explain the SAO amplitude in thermospheric density and compo-
75 sition at solar minimum (G. Cook & Scott, 1966; G. Cook, 1967; G. E. Cook, 1969b).
76 G. E. Cook (1969a) reported on the SAO in mass density at 90 km using rocket data and
77 suggested that the source of T-I SAO is possibly in the mesosphere or the stratosphere.
78 Jacchia (1971) and Jacchia (1977) later updated their thermospheric model such that
79 the T-I SAO was considered as a density variation rather than purely a temperature vari-
80 ation.

81 An internal thermospheric mechanism called the ‘thermospheric spoon’ (TSM) was
82 proposed by T. J. Fuller-Rowell (1998) using the Coupled Thermosphere Ionosphere Model
83 (CTIM) (T. Fuller-Rowell et al., 1996). According to this mechanism, at solstices, due
84 to the tilt of the Earth, the temperature gradient between the two hemispheres results
85 in a global-scale, summer-to-winter interhemispheric circulation. It is also marked by up-
86 welling in the summer and downwelling in the winter. This circulation acts as a large-
87 eddy resulting in a much more mixed thermosphere and a smaller scale height during
88 solstices. Jones Jr., Emmert, et al. (2018) showed using controlled simulations of Ther-
89 mosphere Ionosphere Mesosphere Electrodynamics General Circulation Model (TIME-
90 GCM) that the magnitude of SAO reduces to 2% relative to the annual average when
91 the tilt of the Earth is reduced to 0°, thus proving that the obliquity of the Earth is the
92 largest factor for the SAO in the Earth’s upper atmosphere.

93 The TSM also results in larger densities of lighter species, such as atomic oxygen
94 and helium, in the winter hemisphere (Mayr & Volland, 1972; Mayr et al., 1978; Cageao
95 & Kerr, 1984; T. J. Fuller-Rowell, 1998; Rishbeth & Müller-Wodarg, 1999) via vertical
96 and horizontal transport. The lifetime of O increases to several months in the MLT. As
97 a result, it becomes susceptible to dynamic effects above the MLT region (Brasseur &
98 Solomon, 1984). Higher [O] in the winter have been observed at altitudes as low as 140
99 km (Grossmann et al., 2000). Sutton (2016) showed that the meridional transport of lighter
100 species is linked with vertical upwelling and downwelling in the two hemispheres, along
101 with horizontal divergence and identified these as the primary mechanisms for the ac-
102 cumulation of light species at high winter latitudes.

103 As stated above, the T-I system has many external drivers. One such driver is the
104 lower atmosphere. Soon after its discovery in the upper thermosphere, the SAO was found
105 in the lower thermosphere and near the mesopause (e.g., G. E. Cook, 1969b, 1969a; King-
106 Hele & Kingston, 1968; King-Hele & Walker, 1969; Groves, 1972). Waves propagating
107 up from the lower atmosphere can couple linearly and non-linearly with the background
108 atmosphere or with each other and significantly affect the T-I SAO (Newell, 1966; Vol-
109 land et al., 1972). Eddy diffusion has historically been used in atmospheric models to
110 parametrize the effects of subgrid-scale gravity wave mixing and breaking on the back-
111 ground densities, temperature and winds (Hodges, 1969). Qian et al. (2009) and Qian
112 et al. (2013) using Thermosphere Ionosphere Electrodynamics General Circulation Model
113 (TIE-GCM) observed that the magnitude of SAO in neutral densities, composition, and
114 peak electron density and height can be improved by introducing a seasonal variation
115 in the global eddy diffusion parameter (K_{zz}) (with no variation in latitude, longitude,
116 or solar time) at the lower boundary of the model, with a maxima during solstices (pri-
117 mary maximum during northern hemisphere summer) and minima during the equinoxes.
118 A larger value of K_{zz} in the mesosphere and lower thermosphere (MLT) during the sol-

119 stices will result in higher concentration of molecular species and lower concentration of
120 lighter species, thus, decreasing the O/N₂, mean scale height, and total density in the
121 thermosphere. The amplitude of SAO in K_{zz} has been under investigation by G. Swen-
122 son et al. (2018) and G. R. Swenson et al. (2019). It has recently been realized that the
123 K_{zz} by Qian et al. (2009) represents net cumulative coupling from the lower atmosphere
124 (see Jones Jr. et al. (2017)) as Salinas et al. (2016) found the amplitude of SAO in K_{zz}
125 derived from SABER CO₂ to be much smaller.

126 In fact, Jones Jr. et al. (2017) pointed out that K_{zz} due to gravity waves may not
127 be a primary driver for SAO in the lower thermosphere but may only affect the phase
128 of SAO. Tidal dissipation from the lower thermosphere also affects the T-I SAO (Siskind
129 et al., 2014; Jones Jr. et al., 2017). Jones Jr. et al. (2017) used TIME-GCM to analyze
130 the contribution of different terms in the globally averaged O continuity equation. They
131 found that the SAO in [O] is forced by a cumulative effect of the advective, tidal and dif-
132 fusive transport of O. O is the major species above 200 km, therefore, any long-term vari-
133 ations are directly manifested in neutral and ionospheric densities in the upper atmo-
134 sphere. Jones Jr., Emmert, et al. (2018) suggested that the upper mesospheric O chem-
135 istry might play an important role in the return branch of the thermospheric spoon cir-
136 culation, but recently showed its effects to be negligible on the T-I SAO amplitude (Jones Jr.
137 et al., 2021). Qian et al. (2017) and Qian and Yue (2017) showed that lower thermospheric
138 winter-to-summer residual circulation can also affect the amount of upwelling and down-
139 welling at higher latitudes, thereby affecting the T-I SAO.

140 1.2 Scope and Approach

141 First principles T-I models such as TIE-GCM (Richmond et al., 1992) and Global
142 Ionosphere Thermosphere Model (GITM) (Ridley et al., 2006) have been widely used
143 to study the contribution of the lower atmosphere to T-I SAO (e.g., Qian et al., 2009,
144 2013; Salinas et al., 2016; Wu et al., 2017). This is because their lower boundaries are
145 at roughly 95 km or slightly above, therefore providing an opportunity to study the ef-
146 fect of different (imposed) lower boundary assumptions. Another category of models are
147 the whole atmosphere models, e.g. Whole Atmosphere Model (WAM) and Whole At-
148 mosphere Community Climate Model with thermosphere and ionosphere extension (WACCM-
149 X), that simulate the entire atmospheric column (i.e., ground-to-space) and thus include
150 physical and chemical processes that T-I models do not have. These models are inval-
151 uable in understanding the coupling of lower atmospheric phenomena and the T-I system.
152 The use of both types of models has the potential to significantly advance our under-
153 standing of the contribution of the lower atmosphere to the T-I system. The coupling
154 of the lower atmosphere with an T-I model can be achieved through multiple mechanisms,
155 for example, by specifying large-scale MLT winds, densities and temperatures at the lower
156 boundary, by introducing variations in eddy diffusion parameter, and by including mi-
157 grating and non-migrating tides (and other waves) in the state variables.

158 The motivation for this study is to better understand how the T-I SAO is controlled
159 by the [O] and winds distribution in the MLT region. It is important because the vari-
160 ations due to dynamics in the lower thermosphere map to higher altitudes via diffusive
161 equilibrium (Picone et al., 2013). This goal is achieved through the alteration of GITM's
162 lower boundary, which is typically specified by the empirical model, Mass Spectrome-
163 ter and Incoherent Scatter Radar Model (MSIS). However, there is a huge uncertainty
164 regarding the dynamics, turbulence, neutral densities near the lower boundary of GITM.
165 This is because, the lower boundary of GITM is in the MLT at ~97 km, which lacks long-
166 term, global observations. Therefore, in order to improve the SAO, we use the whole at-
167 mosphere model, WACCM-X as the lower boundary for GITM and compare the effect
168 on the T-I SAO relative to MSIS driven GITM. There is evidence that since WACCM-
169 X includes the physical mechanisms of the lower atmosphere, it best represents the MLT
170 state and thus the thermosphere more accurately (Dunker et al., 2015; McDonald et al.,

171 2015; J. Liu et al., 2018; Qian et al., 2018; Huba & Liu, 2020). The use of WACCM-X
 172 is also motivated by different spatial and temporal variations of [O] in the lower ther-
 173 mosphere between MSIS and WACCM-X. The opposite latitudinal distribution in MSIS
 174 as compared to SABER data and WACCM-X has been previously studied (Malhotra et
 175 al., 2020). At ~ 95 -100 km, MSIS shows a winter maxima, whereas SABER and WACCM-
 176 X show summer maxima (J. P. Russell et al., 2004; Smith et al., 2010; Sheese et al., 2011;
 177 Malhotra et al., 2020). Moreover, the global mean of [O] within WACCM-X in the MLT
 178 is almost 180° out-of-phase with MSIS. We investigate the effects of these opposite lat-
 179 itudinal and temporal [O] variations on the T-I SAO. We also study the effects of hav-
 180 ing no SAO at the lower boundary, and of constraining the dynamics in the lower ther-
 181 mosphere towards WACCM-X. Note that the long-term variability in the MLT states
 182 used in this study from MSIS and WACCM-X have both annual and semiannual compo-
 183 nents (as well as higher order harmonics), and thus, the forcing at the two solstices
 184 is asymmetrical. Therefore, the variability at higher T-I altitudes intrinsically includes
 185 the annual variation as well. Since, our focus in this study is on understanding the am-
 186 plitude and phase of the semiannual component of the intra-annual variability, we will
 187 be primarily discussing and referring to the T-I SAO. The annual component, that is,
 188 the asymmetry between June and December solstices will be explicitly pointed out in
 189 the text and should not be confused with the semiannual component.

190 2 Methodology

191 2.1 Models

192 2.1.1 *Global Ionosphere Thermosphere Model (GITM)*

193 GITM is a physics based first principles model developed at the University of Michi-
 194 gan by Ridley et al. (2006) that self-consistently solves the Navier Stokes equations for
 195 neutral, ion, electron densities, dynamics, and temperatures in the T-I region, without
 196 assuming a hydrostatic equilibrium. It uses a three dimensional spherical grid with lon-
 197 gitude, latitude and altitude as the coordinate system with the lower boundary in the
 198 MLT at ~ 97 km and the upper boundary at ~ 500 -600 km. In its default mode, MSIS
 199 and Horizontal Wind Model (HWM) are used for initial and lower boundary conditions.
 200 The T-I state in GITM depends on the external drivers of the model, such as solar Ex-
 201 treme Ultraviolet (EUV) inputs, solar wind parameters, energetic electron precipitation,
 202 and high latitude electrical fields. It can couple with other empirical and physics based
 203 estimates for these inputs. In the configuration used in this study, GITM uses the Weimer
 204 model (Weimer, 2005) for high-latitude potential, Flare Irradiance Spectral Model (FISM)
 205 EUV model (Chamberlin et al., 2008) for estimates of solar irradiance at different wave-
 206 lengths and NOAA POES hemispheric power-driven model (T. J. Fuller-Rowell & Evans,
 207 1987) for estimates of energetic particle precipitation. The version of HWM used in this
 208 study is HWM14 (Drob et al., 2015). The GITM simulations in this study have a reso-
 209 lution of $2^\circ \times 4^\circ$ (latitude \times longitude), and roughly a third of scale height in altitude.

210 2.1.2 *Whole Atmosphere Community Climate Model with Thermosphere 211 and Ionosphere Extension (WACCM-X)*

212 WACCM-X is a whole atmosphere model that is built on top of the Whole Atmo-
 213 sphere Community Climate Model (WACCM) and covers the atmospheric region from
 214 the surface to the 500-700 km (H. Liu et al., 2010; H.-L. Liu et al., 2018). WACCM it-
 215 self is built on top of the Community Atmosphere Model (CAM) (Lin, 2004) and is a
 216 part of Community Earth System Model (CESM). WACCM-X uses a conventional spa-
 217 tial grid of latitude, longitude and pressure. It includes self-consistent neutral dynam-
 218 ics, electrodynamics, F-region ion transport and solves for ion/electron temperatures.
 219 Gravity waves are parameterized from both orographic and non-orographic sources and
 220 thus can be used for studying the coupling of T-I system with both geomagnetic drivers

221 and the lower atmosphere (H.-L. Liu et al., 2018). In this study, we use WACCM-X 2.0
 222 in the Specified Dynamics (SD) configuration in our simulations and will refer to it sim-
 223 ply as WACCM-X. In the SD configuration, temperature, winds and surface pressure in
 224 the troposphere and stratosphere are specified from the Modern Era Retrospective Anal-
 225 ysis for Research and Applications (MERRA) dataset (Rienecker et al., 2011). The sim-
 226 ulations used in this study have a horizontal resolution of $1.9^\circ \times 2.5^\circ$ (latitude \times longitude).

227 Here we use hourly averaged WACCM-X output files. WACCM-X outputs the mix-
 228 ing ratios of different species on a geographic latitude/longitude grid and pressure lev-
 229 els with temperature, winds, and geopotential height. Total number density is derived
 230 from pressure and temperature using the ideal gas law. Vertical motion (ω) is output
 231 in the units of Pa/s and is converted to vertical wind, W in m/s as follows :

$$W = -\frac{\omega}{\rho g}, \quad (1)$$

232 where ρ is the total mass density and g is the acceleration due to gravity (assumed con-
 233 stant with altitude). Since GITM uses an altitude grid, the logarithm of the WACCM-
 234 X total number density is linearly interpolated to an intermediate altitude grid. This in-
 235 termediate altitude grid is uniformly defined from 95 km to 152.5 km. Other parame-
 236 ters such as mixing ratios, temperature and winds are linearly interpolated onto this al-
 237 titude grid. The mixing ratios and total number densities are then multiplied to output
 238 the number density for each species on this new grid. The WACCM-X outputs on the
 239 altitude grid are then used in GITM, the specifications of which differ between differ-
 240 ent simulations used in this study. Further details of these simulations are discussed in
 241 Section 2.2.

242 *2.1.3 Mass Spectrometer and Incoherent Scatter Radar Model*

243 The MSIS-class models (Hedin et al., 1977; Hedin, 1983, 1987, 1991) are empiri-
 244 cal models of composition, temperature, and neutral density of Earth’s atmosphere, de-
 245 rived from ground, rocket and satellite-based measurements. MSISE-86 covers the al-
 246 titude region from 90 km to the exobase, while MSISE-90 has the lower boundary at the
 247 surface. These models were a significant improvement over the Jacchia-class models, which
 248 were also empirical models that estimated total mass density from orbital decay of ob-
 249 jects that flew from 1961-1970 (Jacchia, 1965, 1970, 1971). NRLMSISE-00 (Picone et
 250 al., 2002) also extends from the ground to the exobase and includes additional data span-
 251 ning 1965-1983 from the Jacchia models. This includes data from satellite accelerom-
 252 eters, incoherent scatter radars, mass spectrometers, solar ultraviolet occultation, and
 253 drag measurements up to the mid-to-late 1990s. It also contains more data covering high
 254 latitudes and extreme cases of geomagnetic forcing. In this study, we use NRLMSISE-
 255 00 for the lower boundary condition in GITM. A new, improved NRLMSIS 2.0 model
 256 (J. T. Emmert et al., 2020), that ingests SABER [O] measurements has recently been
 257 released, and much better represents MLT [O]. At the time of writing this manuscript,
 258 all the simulations were already completed with the NRLMSISE-00. We do plan to change
 259 the lower boundary in GITM to NRLMSIS 2.0 in the future. In this manuscript, we will
 260 refer to NRLMSISE-00 simply as MSIS.

261 **2.2 GITM Simulations**

262 The GITM simulations used in this study are for 2010 and use measured time-varying
 263 geospace indices to specify high-latitude and solar EUV drivers so that the results can
 264 be validated against observational datasets. This year was chosen because it was a ge-
 265 omagnetically quiet year during a solar minimum, which emphasizes the lower atmospheric
 266 effects on the upper thermosphere. The lower boundary of GITM is controlled by two
 267 ghost cells in altitude below 100 km which are filled with densities, temperatures and
 268 winds. These are then used in the solvers for the first couple of lower cells in GITM, so

269 that they control the dynamics in these cells. Table 1 summarizes these simulations. All
270 these simulations use a K_{zz} value of $300 \text{ m}^2/\text{s}$ that is constant with time.

271 The default configuration is the G/MSIS simulation. In this configuration, for neu-
272 tral densities, only the second ghost cell nearest to 100 km is specified from MSIS. For
273 the first cell, a hydrostatic solution for most neutral densities is projected from the sec-
274 ond cell so as to not drive constant non-zero acceleration. [O] and T are specified from
275 MSIS and kept the same in both the cells. Horizontal winds are specified by HWM in
276 the second cell and determined in the first cell similar to densities using the gradients
277 from cells above. Since HWM only has horizontal winds, the vertical velocity for all species
278 is determined in both the cells so as to have zero flux through the lower boundary, i.e.,
279 the value in the first (second) ghost cell is the opposite of the value in the second (first)
280 real cell. In the second simulation, G/NOSAO, we use GITM in its default configura-
281 tion, but MSIS has the AO and SAO flags turned off for both symmetrical and asym-
282 metrical components. The horizontal winds in the second cell are zero. In the first cell,
283 they are non-zero and determined as discussed above.

284 In the third simulation, G/WX, we use WACCM-X as the lower boundary condi-
285 tion. For densities, similar to the default configuration, values are specified in the sec-
286 ond cell only and hydrostatic condition is enforced in the first cell. [O] is same in both
287 the cells. However, for winds (including the vertical winds) and temperatures, values are
288 specified in both the cells from WACCM-X. Thus, there is a vertical flux of winds and
289 temperature in this simulation, resembling more realistic atmospheric conditions.

290 In the fourth simulation, G/NUDGE, the lower boundary conditions are identical
291 to the G/WX simulation, but from 100 km to 140 km, GITM winds (full dynamical fields)
292 are nudged towards WACCM-X winds. The vertical weighting function (ζ) for the nudg-
293 ing is similar to that used by Maute et al. (2015) and is as follows :

$$\zeta = \cos^2 \left[\frac{\pi}{2} \left(\frac{z - z_{lb}}{z_{max} - z_{lb}} \right) \right], \quad (2)$$

294 where z_{lb} and z_{max} are 100 km and 140 km, respectively. The nudging technique is sim-
295 ilar to that used by Wang et al. (2017) :

$$X(\lambda, \theta, z, t) = (1 - \alpha\zeta(z))X_G(\lambda, \theta, z, t) + \alpha\zeta(z)X_W(\lambda, \theta, z, t), \quad (3)$$

296 where X represents zonal wind, meridional wind and vertical wind fields. X_G and X_W
297 represents the model fields from GITM and WACCM-X, respectively. In this technique,
298 the GITM fields are constrained by the dynamics fields of equation 3. The use of ver-
299 tical profile implies that nudging is the strongest at 100 km and weakest at 140 km. This
300 allows for a smooth transition from WACCM-X lower thermospheric dynamics to GITM
301 dynamics in this simulation. α represents the relaxation factor and was discussed in de-
302 tail by Jones Jr., Drob, et al. (2018), and is defined as -

$$\alpha = G\Delta t, \quad (4)$$

303 where G represents the inverse of relaxation time. $\alpha=1$, implies that GITM fields are
304 overwritten at every model time-step. Here we use a relaxation time of 60s. The model
305 time-step, Δt in GITM varies and is on average $\sim 2\text{s}$. This implies α would on average
306 have a value of ~ 0.03 .

307 2.3 Datasets

308 We use a number of different datasets to validate the phase and amplitude of T-
309 I SAO produced by the different simulations.

2.3.1 *Sounding of the Atmosphere using Broadband Emission Radiometry (SABER)*

SABER is an instrument on NASA's Thermosphere Ionosphere Mesosphere Energetics Dynamics (TIMED) satellite. SABER provides global vertical profiles of temperature, pressure, geopotential height, volume mixing ratios, volume emission rates, and cooling and heating rates for several trace species in the MLT region (Mlynczak, 1996, 1997; Russell III et al., 1999; Yee, 2003). The version of the dataset used in this study is V2.0 (Panka et al., 2018). We use 10-year averaged [O] data to understand its temporal and spatial distribution at 97 km. Averages for each year are derived by binning the data into a day of the year and latitude grid. Then, 10 years of data are averaged together.

2.3.2 *Global Ultra-Violet Imager (GUVI)*

GUVI is a UV spectrograph with primary objectives of measuring thermospheric composition, temperature, and high-latitude particle precipitation (Paxton et al., 1999; Christensen et al., 2003; Yee, 2003). In this study, we use the height-integrated O/N₂ derived from GUVI measurements. Integrated O/N₂ is defined as the ratio of integrated O to N₂ column densities, from the top of the atmosphere as defined by a model or the altitude of the satellite, downward until the altitude where the N₂ column integrated density reaches 10²¹ m⁻² (Strickland et al., 1995). We will henceforth refer to it simply as O/N₂. In this study, we use the global average for 2010. It is derived by binning the data into a day of the year and latitude grid. We use the level 3 GUVI data product.

2.3.3 *TIMED Doppler Interferometer (TIDI)*

TIDI is a Fabry-Perot interferometer that measures global horizontal winds in the MLT region (Yee, 2003). In this study, we use TIDI data for 2010 to validate the meridional winds in the lower thermosphere. A 60-day average is determined after binning the data into an altitude and latitude grid. Level 3 vector data is used here.

2.3.4 *Global Navigation Satellite System (GNSS)*

GNSS data is used to determine the line-integrated ionospheric electron density by measuring the propagation time difference between two different radio frequencies (Vierinen et al., 2016). The measurements are scaled by 10¹⁶m⁻², also referred to as total electron content (TEC) units. This slant ionospheric TEC is converted into vertical total electron content (VTEC) by using a scaling factor proportional to the elevation angle of the satellite from the receiver (Vierinen et al., 2016). The data that we use here has a spatial resolution of 1° × 1° and a temporal resolution of 30 minutes. In this study, we use the global mean TEC for 2010 for validation of the ionospheric SAO. It is derived by binning the data into a day of the year and latitude grid.

2.3.5 *Challenging Minisatellite Payload (CHAMP) and Gravity Recovery and Climate Experiment (GRACE)*

CHAMP and GRACE are low-earth orbit satellites with a primary objective of making accurate measurements of Earth's gravity field (Reigber et al., 2002; Tapley et al., 2004). They have highly accurate accelerometers that have been widely used to derive neutral density measurements from atmospheric drag measurements (e.g., Lühr et al., 2004; S. Bruinsma et al., 2004; Sutton, 2011). In this study, we use neutral mass density datasets from 2007-2010 from these satellites to validate the mass density SAO in the upper thermosphere. Averages for each year were derived by binning the data into a day of year and latitude grid.

2.3.6 Emmert Dataset

J. T. Emmert (2015) studied the trends in globally averaged neutral mass density from 1967-2013. This dataset is derived from the orbits of ~ 5000 objects between the altitude of 200-600 km (J. T. Emmert, 2009). This data has a resolution of 3-6 days with daily relative accuracy of $\sim 2\%$ and absolute accuracy of 10%. In this study, we use the derived density data for 2010 at 400 km. We will henceforth refer to this dataset simply as ‘Emmert ρ ’ or ‘Emmert dataset’.

3 Results

3.1 Motivation

Figure 1 shows the normalized integrated O/N₂, integrated vertical TEC and mass density (ρ) for G/NOSAO and G/MSIS simulations, compared with different observational datasets and empirical models for 2010. The thin lines are the daily averages for all data, and the thicker lines indicate fitted values. The fitted curves are derived by fitting a least squares annual and semiannual variation to the data. The red vertical lines indicate the solstices and equinoxes. All the values are normalized as specified below,

$$v_{norm} = \frac{v - \bar{v}}{\bar{v}} \times 100, \quad (5)$$

where \bar{v} represents the global annual average of value, v (where v is ρ , TEC or O/N₂). In Figure 1a, an SAO with equinoctial maxima and an amplitude of 18% (with respect to its annual average) is observed in the GUVI O/N₂ data. The amplitude of SAO for different data are determined by fitting a semiannual variation. Since, O/N₂ is an integrated value, it largely reflects the lower T-I state at ~ 140 km, as the densities decrease exponentially with altitude (Yu et al., 2020). G/NOSAO shows smaller SAO amplitude as compared to G/MSIS, which is in better agreement with the GUVI data and pure MSIS, thus demonstrating the importance of appropriate lower boundary SAO. The amplitude of SAO for GUVI is larger than that of MSIS. We can also compare the SAO phase of different simulations by analyzing their day of maxima and minima. The phase of both the simulations agrees well with the observations.

Figure 1b shows TEC for the two simulations compared with GNSS data. TEC being an integrated quantity has the largest contribution from the peak electron density altitude at ~ 250 -300 km. The SAO amplitude in GNSS TEC data is $\sim 13\%$, which is consistent with the climatological value calculated by J. T. Emmert et al. (2014). This is much less than that observed in GUVI O/N₂. Similar to Figure 1a, using MSIS as the lower boundary increases the SAO amplitude in GITM. There is also a small phase difference between the simulations and the GPS data, with GITM leading (peak earlier in the year) the data during March and June. G/MSIS lags behind the G/NOSAO, and is in better agreement with the phase of GNSS data.

Figure 1c shows the mass densities at ~ 400 km for both the simulations compared with those from the CHAMP and GRACE satellites (normalized at 400 km). The densities for CHAMP and GRACE are averaged between 2007-2010 because of data gaps in 2010. We also show values from the Emmert dataset and the MSIS empirical model. In this altitude region, G/NOSAO and G/MSIS show agreement in both the SAO phase and amplitude. CHAMP and GRACE mass densities also agree well with each other. The largest disagreement is in the phase of the SAO. Both the model simulations lead the observations and empirical model, especially during June and September. Comparing with the Emmert data, GITM simulations have smaller deviations from the mean. An equinoctial asymmetry is also prominent in ρ and not as much in O/N₂ and TEC. MSIS, Emmert data and GITM simulations have larger (smaller) densities during September (March) equinox, whereas CHAMP and GRACE have smaller (larger) values during this time. A similar observation was made by Lei et al. (2012) in the CHAMP and

404 GRACE data, namely that the densities are larger during March than those around Septem-
 405 ber during periods of high and moderate solar activity. Since CHAMP and GRACE data
 406 are averaged for 2007-2010, it is possible it does not accurately represent the thermo-
 407 spheric state during a geomagnetic quiet time (2010 for our purposes).

408 Note the phase of GUVI and GNSS data leads the CHAMP data, indicating that
 409 there is a phase progression in the T-I SAO with altitude that GITM is unable to cap-
 410 ture. For example, GUVI and GPS data show a September maxima closer to equinox
 411 (day 266), whereas, the September maximum for CHAMP ρ is around day 280-300. More-
 412 over, the phase progression with altitude is not uniform for different times of the year,
 413 and is more prominent during June and September. This is different from the inference
 414 by Yue et al. (2019) as they observed that the phase of the SAO in height-resolved O/N₂
 415 stays the same between the lower and upper thermosphere. An annual asymmetry is also
 416 quite noticeable for all the parameters shown in Figure 1. Lower O/N₂, TEC, and ρ are
 417 observed near June solstice as compared to the December solstice. Another interesting
 418 observation is that G/MSIS (the simulation in better agreement with the observational
 419 datasets), has smaller SAO amplitude than GUVI O/N₂ and Emmert ρ dataset, but larger
 420 than GNSS TEC. The phase difference between the simulated SAO in G/MSIS and obser-
 421 vational datasets is much larger for ρ , and smaller for O/N₂, and TEC. This obser-
 422 vation delineates the challenge of the model-data comparison studies, and a possible rea-
 423 son might be inherent biases and uncertainties in different satellite datasets.

424 These results reveal that GITM is able to reproduce SAO in some of the T-I pa-
 425 rameters, TEC and ρ at 400 km without necessarily having an SAO at the lower bound-
 426 ary, but with lower amplitude and shifted phase. However, the SAO in composition, O/N₂
 427 is much smaller, but not absent. This is not necessarily the case with other T-I models
 428 whose lower boundaries are between 95-100 km (e.g. TIE-GCM see Qian et al. (2009)
 429 and Jones Jr. et al. (2021)). In the absence of a composition or eddy diffusion SAO im-
 430 posed at the model lower boundary, the only major driver of the SAO is the thermospheric
 431 spoon mechanism. The SAO in TEC and ρ are also influenced by factors other than com-
 432 position such as the transport, plasma scale height for TEC, and temperature for ρ . To
 433 eliminate the disagreements in the SAO amplitude and phase, the contribution from the
 434 lower atmosphere cannot be ignored. In the next section, we discuss the distribution of
 435 [O] in the MLT.

436 3.2 Lower Boundary Conditions

437 Figures 2a and 2b show 10-year averaged O number density from SABER at 85 km
 438 and 97 km, while Figures 2c and 2d show the area-weighted global averages at each alti-
 439 titude. The global averages are only for the latitude region spanning $\pm 55^\circ$ because of
 440 missing data at high latitudes. Using a longer term average for satellite data reduces bi-
 441 ases due to incomplete longitudinal sampling, tidal phases, missing data, etc, thus in-
 442 creasing the statistical significance.

443 The latitudinal distribution of [O] reverses between the two altitudes, consistent
 444 with what Smith et al. (2010) showed using an earlier version of the SABER [O] data.
 445 At 85 km, the higher latitudes show an annual variation with larger [O] during winter.
 446 This is because of the gravity wave induced summer-to-winter meridional circulation in
 447 the mesosphere, and downwelling in winter (e.g., Lindzen, 1981; Holton, 1983; Garcia
 448 & Solomon, 1985). The lower latitudes show an SAO with maxima around the equinoxes
 449 which is similar to the mesospheric semiannual oscillation (MSAO) in zonal winds in the
 450 equatorial mesosphere (Garcia et al., 1997). The SAO in zonal winds has been found to
 451 be driven by momentum deposition by gravity waves that are selectively filtered by the
 452 stratospheric winds (Burrage et al., 1996). However, the mechanism for the SAO at 85
 453 km in [O] is still under investigation. The lifetime of O in this altitude region is too short
 454 to be affected by a wind circulation of such a long period. Smith et al. (2010) suggested

455 that the seasonal variation in the amplitude of the migrating diurnal tide might be a more
456 likely source. It was demonstrated by Jones Jr. et al. (2014) that tides induce a net in-
457 crease in [O] during equinoxes close to the equator via tidally induced advective trans-
458 port. Figure 2c shows that at 85 km, the global average is dominated by the SAO with
459 maxima closer to the equinoxes. This is because the high latitude AO in both the hemi-
460 spheres is out of phase and cancels out, which then reinforces the lower latitudinal SAO
461 in the global means.

462 At 97 km, the AO at higher latitudes reverses with larger [O] during the summer
463 (J. P. Russell et al., 2004; Smith et al., 2010; Sheese et al., 2011; Malhotra et al., 2020).
464 The mechanism responsible for these summer maxima is still under investigation (Smith
465 et al., 2010; Qian et al., 2017; Rezac et al., 2015; Malhotra et al., 2020). The effect of
466 this reversal on the upper thermosphere was discussed by Malhotra et al. (2020). It can
467 also be observed that the SAO at 97 km at lower latitudes is almost non-existent, and
468 is smaller than that observed by Smith et al. (2010). This difference might arise because
469 of different years that are included in the averages or different versions of SABER data.
470 In Figure 2d, a small intra-annual variation is observed with maxima around solstices
471 in the global mean [O]. The high latitude AO in the two hemispheres do not completely
472 cancel each other out, resulting in net maxima closer to the solstices. It should be noted
473 that these plots represent averaged values over a 10 year period. The global averages for
474 individual years can have deviations from this average. The amplitude of smoothed intra-
475 annual variation is $\sim 20\%$ at 85 km and decreases to $< \sim 3\%$ at 97 km. Note that if high
476 latitude SABER data is also included in the calculation of global average [O], this am-
477 plitude increases and SAO peaks a little later in the year.

478 Figures 3a and 3b illustrate the latitudinal distribution of [O] at ~ 97 km from MSIS
479 and WACCM-X in 2010, respectively. WACCM-X shows more temporal and spatial vari-
480 ations, which is indicative of atmospheric variations including gravity waves, non-migrating
481 tides, and planetary waves propagating up from the lower atmosphere. The latitudinal
482 distribution of [O] in WACCM-X matches better with the SABER data at 97 km in Fig-
483 ure 2b. Both show annual variation at higher latitudes with maxima in summer and min-
484 ima in winter. MSIS, on the other hand, has higher [O] during winter. This is because
485 the [O] for MSIS in the MLT is extrapolated from higher altitudes assuming mixed equi-
486 librium below the turbopause (~ 105 km) with a correction factor for chemistry and dy-
487 namics. The version of MSIS used here, NRLMSISE-00 did not have [O] observations
488 in the MLT region as SABER had not been launched when it was created. Most of the
489 observations in this region are of neutral densities and temperature from rockets and in-
490 coherent scatter radars. Therefore, the correction factors in MSIS do not account for the
491 processes responsible for high latitude summer [O] in the MLT. The summer MLT max-
492 imum in [O] at high latitudes is better represented in NRLMSIS 2.0 (see Figure 11 of
493 J. T. Emmert et al. (2020)). At low latitudes, WACCM-X and MSIS show a larger am-
494 plitude SAO than what SABER observed. A possible explanation for this might be the
495 larger uncertainty in SABER [O] at these altitudes (Mlynczak et al., 2013; Smith et al.,
496 2013).

497 Figure 3c compares the area-weighted global mean [O] for MSIS, WACCM-X and
498 SABER data at 97 km. The [O] for MSIS and WACCM-X is for 2010, whereas the SABER
499 data is the average for 2002-2011 shown previously in Figure 2d. The global mean [O]
500 for both SABER and WACCM-X shows an SAO with maxima closer to solstices, whereas
501 [O] for MSIS shows an SAO with 180 degree phase shift (maxima around equinoxes). In
502 MSIS, the high latitude AO in both the hemispheres cancels out with each other result-
503 ing in minima at solstices. For WACCM-X, at equinoxes, low [O] at mid-to-high latitudes
504 result in minima at equinoxes relative to solstices. The SAO amplitude is lower and also
505 in agreement between WACCM-X and SABER. The overall magnitude of [O] for SABER
506 however exceeds that of both MSIS and WACCM-X. Note, NRLMSIS 2.0 [O] at 97 km

507 are roughly a factor of 2 higher than what is shown in Figure 3c (see J. T. Emmert et
508 al. (2020) Figures 11-13).

509 Since the latitudinal distribution of [O] for WACCM-X is similar to SABER, the
510 lower boundary of GITM was changed to WACCM-X in 2010 to assess its effects on the
511 T-I SAO. We cannot directly use SABER at the lower boundary of GITM because of
512 the lack of measurements at high latitudes. As specified in Section 2, we also use other
513 parameters from WACCM-X in GITM. The temporal and latitudinal variation for these
514 parameters are not much different between MSIS and WACCM-X, and are shown in the
515 supporting information. Therefore, our results primarily signify the implications of dif-
516 ferent [O] distribution at the lower boundary. In the next few sections, we will analyze
517 the results of different simulations, starting with a comparison of meridional winds in
518 the thermosphere.

519 3.3 Dynamics

520 Figure 4 shows the 16-day averaged meridional winds for HWM, WACCM-X and
521 different GITM simulations at June solstice (June 21 ± 8 days). We take a multi-day av-
522 erage to eliminate short term variations due to tides and planetary waves, such that the
523 winds in this figure represent background meridional winds. All GITM simulations ex-
524 cept G/NUDGE show a higher altitude summer-to-winter thermospheric circulation start-
525 ing from around ~ 140 km which roughly agrees with HWM and WACCM-X winds. Both
526 HWM and WACCM-X although have larger wind speeds at summer high latitudes. G/NUDGE
527 shows equatorward winds between 140-170 km and summer-to-winter winds above 170
528 km. The wind patterns in the lower thermosphere are much different between the dif-
529 ferent model runs. In the lower thermosphere, between 100-120 km, two equatorward
530 circulation cells are observed in G/NOSAO, G/MSIS, and G/WX simulations. These
531 circulation cells are observed in GITM throughout the year and were shown to be driven
532 by the centrifugal force (Malhotra et al., 2020). Comparing Figures 4d and 4e, we see
533 that changing the lower boundary from MSIS to WACCM-X affects the magnitude of
534 the winds in the lower thermosphere, but does not change their direction. HWM and WACCM-
535 X winds, on the other hand, show a region with winter-to-summer circulation which has
536 previously been observed to be caused by residual gravity waves during solstices (Qian
537 et al., 2017). HWM primarily has Wind Imaging Interferometer (WINDII) data in this
538 altitude regime. Being a global T-I model, GITM does not resolve gravity waves. There-
539 fore, it does not have the requisite forcing for this opposite lower thermospheric cir-
540 culation, and hence relies on realistic boundary conditions. G/NUDGE demonstrates the
541 effect of constraining the winds in GITM with WACCM-X up to 140 km. Between 100-
542 120 km, G/NUDGE shows weak winter-to-summer circulation similar to pure WACCM-
543 X and HWM.

544 As an aside, during equinoxes (not shown here), GITM simulations continue to show
545 the equatorward circulation cells below 120 km. During this time, HWM and WACCM-
546 X also show a similar circulation pattern. This has also been previously observed in the
547 High Resolution Doppler Imager (HRDI) and WINDII wind measurements onboard the
548 Upper Atmosphere Research Satellite (UARS) (McLandress et al., 1996; Zhang et al.,
549 2007). It is possible that, because of absence of strong residual gravity wave forcing dur-
550 ing equinoxes, the centrifugal force dominates the momentum budget in this region at
551 equinoxes, resulting in net equatorward winds in the lower thermosphere.

552 Figure 5 shows the 60-day-averaged meridional wind for TIDI data near Decem-
553 ber and June solstices. In Figure 5a, between 90-100 km, northward winds indicate the
554 mesopause summer-to-winter circulation during December solstice. The horizontal line
555 at 97 km indicates the lower boundary of GITM. Above 100 km, southward winds de-
556 pict the winter-to-summer residual circulation. Similar meridional wind patterns are also
557 observed during June solstice in Figure 5b in the opposite direction, potentially signi-

558 fying an AO in meridional winds in the lower thermosphere. Recently, Dhadly et al. [2020]
 559 showed similar oscillations at midlatitudes, as well as an SAO, and high order intra-annual
 560 oscillations in middle thermospheric in situ measurements of the horizontal neutral winds
 561 from the Gravity Field and Steady-State Ocean Circulation Explorer (GOCE) accelerom-
 562 eter. HWM and WACCM-X agree with the TIDI data between 100-120 km, and thus
 563 nudging the GITM dynamics towards WACCM-X should improve the thermospheric mod-
 564 eling and SAO in GITM. However, it is worth noting that the magnitude of the winds
 565 in the winter-to-summer circulation is much larger in TIDI data during both solstices.
 566 In the next section, we will reveal the effect of different thermospheric dynamics on the
 567 amplitude and phase of T-I SAO of the simulations.

568 3.4 Global Mean Intra-Annual Variations

569 Figure 6 reveals the averaged normalized O/N_2 , TEC, and $[O]$ and ρ at ~ 400 km
 570 for GITM simulations compared with different datasets and models for 2010. This com-
 571 parison was shown for G/NOSAO and G/MSIS previously in Figure 1. Similar to Fig-
 572 ure 1, thin lines are the daily averages for all data, and the thicker lines indicate fitted
 573 values. The parameters are normalized with respect to annual means as specified in equa-
 574 tion 5. The amplitudes and phases for different model runs and observations are also sum-
 575 marized in Table 2.

576 Figure 6a shows the daily averaged and fitted O/N_2 . The black line represents the
 577 averaged O/N_2 measurements from GUVI data. The phase of the SAO in G/MSIS and
 578 G/NOSAO match best with the GUVI data and the MSIS model, with equinoctial max-
 579 ima. Using MSIS at the lower boundary (G/MSIS) is however not enough, as it produces
 580 a smaller SAO amplitude in comparison to GUVI observations. While WACCM-X $[O]$
 581 compares well with SABER in the MLT, using WACCM-X at the lower boundary of GITM
 582 (G/WX) leads to a T-I SAO with maxima closer to solstices and a phase difference of
 583 $\sim 180^\circ$ from GUVI SAO. Using dynamics from WACCM-X in the lower thermosphere
 584 (G/NUDGE) reduces the amplitude of this out-of-phase SAO, but does not completely
 585 correct it.

586 The phase shifts and amplitudes in TEC, and globally averaged $[O]$ and ρ in Fig-
 587 ures 6b, c and d show similar model differences as the O/N_2 , with maxima and minima
 588 for G/WX and G/NUDGE almost midway between solstices and equinoxes. At 400 km,
 589 the major neutral constituent is O, and thus, ρ primarily represents variations in $[O]$.
 590 However, for neutral density at 400 km, there are more observational datasets to vali-
 591 date the simulations against. The densities from Emmert dataset, CHAMP and GRACE
 592 peak around equinoxes (with an equinoctial asymmetry) similar to that of G/NOSAO
 593 and G/MSIS. The difference in phase of both G/WX and G/NUDGE simulations with
 594 respect to G/MSIS in Figures 6b, c, d is lower when compared to that for O/N_2 in Fig-
 595 ure 6a. This hints towards phase progression of SAO with altitude in G/WX and G/NUDGE
 596 simulations towards equinoctial maxima due to the effect of temperature and possibly
 597 the thermospheric spoon mechanism. This can be also noted by comparing the day of
 598 first maxima of G/WX and G/NUDGE simulations for different quantities in Table 2.
 599 The summer-to-winter meridional wind speeds increase with altitude in the lower-middle
 600 as shown in Figure 4, resulting in decrease of global mean solstitial densities relative to
 601 equinoctial densities. This will be more clear in Figure 7 where we show variations in
 602 phase of SAO with altitude.

603 The WACCM-X model also has an SAO that is out-of-phase in the lower thermo-
 604 sphere as seen in O/N_2 (Figure 6a). However, it has the correct phase in TEC, $[O]$, and
 605 ρ at 400 km, with peaks at the equinoxes. This implies that the phase shifts towards equino-
 606 ctial maxima in the lower-middle thermosphere. Nudging GITM dynamics to WACCM-
 607 X up to 140 km reduces the amplitude of oppositely-phased SAO in G/NUDGE, but is
 608 not enough to completely correct the phase and shift the phase to equinoctial maxima.

609 This reduction in the amplitude of the opposite SAO signifies primarily the contribu-
 610 tion of the lower thermospheric residual circulation. Qian and Yue (2017) showed that
 611 the residual circulation results in upwelling and reduction of O/N₂ in winter, and down-
 612 welling and its increase in summer. This leads to an overall reduction of the global mean
 613 O/N₂ by 18% during solstices. Comparison of G/NUDGE with G/WX shows a similar
 614 reduction in the global mean for all parameters in Figure 6 around both June and De-
 615 cember solstices. Further explanation of these differences is beyond the scope of this manuscript.

616 Figure 7 compares the altitudinal progression of the [O] and ρ SAO amplitudes and
 617 phases. For [O] at 100 km, MSIS and G/MSIS have the largest amplitude of 15%, with
 618 maxima at around equinoxes (day 100). Both G/WX, G/NUDGE and the WACCM-
 619 X model start with a much lower amplitude of around 5%, with maxima near solstices
 620 (day 10), which are in better agreement with the amplitude and phase of SABER data
 621 at 100 km. G/NOSAO starts with an amplitude of ~ 0 . WACCM-X shows a minimum
 622 at around ~ 120 km, above which the amplitude increases monotonously. The amplitude
 623 of SAO in WACCM-X remains lower than other simulations also causing much lower am-
 624 plitude in G/NUDGE, at ~ 10 -15%. WACCM-X transitions from solstitial maxima to
 625 equinoctial maxima in the 100-200 km altitude region. In the upper thermosphere, G/MSIS,
 626 G/NOSAO and G/WX have the largest amplitudes of $\sim 25\%$, which is greater than that
 627 of MSIS. Since, there are limited observations of [O] in the thermosphere, there is an un-
 628 certainty regarding which simulation represents the correct SAO amplitude. A similar
 629 amplification of the SAO with altitude for different neutral species was depicted by Picone
 630 et al. (2013) because of the variation in temperature. Thus, it is possible that different
 631 temperature structure between the simulations leads to different amplification factors
 632 of the SAO. When considering the importance of SAO at the lower boundary, G/NOSAO
 633 catches up with other simulations above 300 km. However, the absence of lower bound-
 634 ary SAO results in much smaller amplitude below 300 km. Hence, our results indicate
 635 that it is necessary to have an SAO in composition and winds at the lower boundary of
 636 T-I models for better agreement with the observations in the lower-middle thermosphere,
 637 otherwise it can lead to underestimation of the SAO in this region. Recent work by Jones Jr.
 638 et al. (2021) using the TIE-GCM showed that including NRLMSIS 2.0 composition im-
 639 proved the globally-averaged mass density SAO at 400 km in the TIE-GCM (although
 640 the TIE-GCM amplitude was notably smaller than observed).

641 The phase for [O] largely remains constant with altitude for all GITM simulations.
 642 G/MSIS and G/NOSAO continue to have maxima at equinox in the upper thermosphere,
 643 which leads the MSIS SAO, as observed previously in Figure 1c. G/WX and G/NUDGE
 644 have maxima near the solstices progressing towards equinoxes with altitude. As stated
 645 before, we believe that this is due to the effect of temperature and the summer-to-winter
 646 thermospheric circulation that pushes the thermosphere towards a more mixed state at
 647 solstices. This phase progression is most apparent between 100-300 km, above which it
 648 does not change much. This is because the thermospheric spoon mechanism is more dom-
 649 inant in this altitude region. Above ~ 300 km, O is in diffusive equilibrium and thus the
 650 SAO phase is constant at higher altitudes.

651 Figure 7b shows the variation of SAO phase and amplitude for ρ . Above 200 km,
 652 O is the major species and hence the SAO in ρ primarily reflects the variations in [O].
 653 At 100 km, all the simulations start with a maxima at \sim day 90 (equinox) because of the
 654 dominance of the N₂ density. The SAO in ρ for G/MSIS and G/NOSAO has almost a
 655 constant phase with altitude displaying an equinoctial maxima, fairly consistent with MSIS
 656 and TIME-GCM simulations by Jones Jr. et al. (2017). Pure WACCM-X also exhibits
 657 a constant SAO phase above 100 km, peaking at equinox. This is because of the dom-
 658 inant equinoctial maxima in N₂ in the lower-middle thermosphere and equinoctial max-
 659 ima in [O] above 200 km. In G/WX and G/NUDGE, the phase shifts from equinoctial
 660 (due to N₂) towards solstitial maxima at ~ 200 -250 km (because of O). The model runs
 661 that show the correct phase, i.e., the equinoctial peaks (WACCM-X, G/MSIS, G/NOSAO),

662 lead all observational datasets (MSIS, CHAMP, GRACE, Emmert data, and GOCE).
 663 These observational datasets peak at a similar time around \sim day 100, while model sim-
 664 ulations peak at \sim day 80 (also in Table 2). The SAO amplitude for ρ increases with alti-
 665 tude similar to that of [O]. The SAO amplitude for the GITM simulations reaches a
 666 maximum of \sim 20% and is in better agreement with CHAMP and GRACE, whereas the
 667 amplitude is much larger in the Emmert and GOCE data. The SAO in temperature at
 668 400 km (not shown here) has an amplitude of \sim <3%, maximizing around \sim day 70-80
 669 for G/NOSAO and G/MSIS and \sim day 50-60 for G/WX and G/NUDGE.

670 In summary, using WACCM-X [O] instead of MSIS at the lower boundary in GITM,
 671 leads to the phase of T-I SAO that does not agree with the observations, despite the SABER-
 672 like [O] distribution at the lower boundary. This can be linked with the solstitial peaks
 673 in the global mean of [O] at 97 km in WACCM-X. Even though, O is not in diffusive equi-
 674 librium above 97 km, but in fact is driven by the dynamics and chemistry in the lower
 675 thermosphere, the phase shift in SAO between the MLT and upper thermosphere is marginal.
 676 The maximum change in the phase of SAO in global mean [O] in GITM between the lower
 677 boundary and upper thermosphere is \sim 30 days, and thus is not enough to drive a sea-
 678 sonal change in the phase of SAO, i.e., from solstices to equinoxes.

679 A similar analysis was done by Jones Jr. et al. (2017) (see Figure 2) for different
 680 TIME-GCM simulations. Table 2 shows the SAO amplitudes and phases for standard
 681 TIME-GCM and TIE-GCM with Qian et al. (2009) eddy diffusion variation (TIE-GCM
 682 w/ Q09). Comparing with our G/MSIS simulation, for both TEC and ρ at 400 km, G/MSIS
 683 peaks earlier in the year (day 83) as compared to these two simulations from Jones Jr.
 684 et al. (2017) (day 106 and 122). The phase of the observations (GPS, CHAMP, GRACE,
 685 and Emmert dataset) lies between these different models. For the SAO amplitudes, these
 686 three model runs have larger amplitudes than the GNSS TEC (\sim 13%). Comparing the
 687 ρ at 400 km, both TIE-GCM w/ Q09 and G/MSIS agree with the SAO amplitude of CHAMP
 688 and GRACE (\sim 16-17%). To further understand the differences between our simulations,
 689 we will analyze the latitudinal distribution of thermospheric densities in the next sec-
 690 tion.

691 3.5 Global Distribution

692 Figure 8 illustrates the latitudinal distribution of [O] at \sim 150 km. G/NOSAO and
 693 G/MSIS show a similar variation, with equinoctial maxima at lower latitudes. At sol-
 694 stices, larger [O] is observed in the winter hemisphere because of the interhemispheric
 695 summer-to-winter circulation. At \sim day 180, by comparing the summer minima in the
 696 northern hemisphere between these two simulations, we see that G/MSIS has a minima
 697 spanning a larger latitudinal region. Similar behavior is observed starting from \sim day 350
 698 in the southern hemisphere. This is because G/MSIS starts with the summer minima
 699 and winter maxima at the GITM lower boundary (see Figure 3). The interhemispheric
 700 circulation adds to this depletion in summer and accumulation in winter. This can re-
 701 sult in an underestimation and overestimation of [O] in summer and winter, respectively
 702 (Malhotra et al., 2020).

703 G/WX and G/NUDGE also show winter [O] accumulation. Thus, GITM is able
 704 to reverse the opposite latitudinal variation of [O], from larger values in the summer at
 705 \sim 97 km to relatively larger values in winter at \sim 150 km. There is also an increase in sum-
 706 mertime [O], and thus decrease in the summer-to-winter gradient at solstices similar to
 707 G/NOSAO. The features of primary importance in these figures (8c and 8d) are the low
 708 latitude maxima at solstices that contribute to the global mean T-I SAO that is almost
 709 oppositely-phased with respect to the observations and G/MSIS (shown in Figure 6). G/NUDGE
 710 has a similar latitudinal distribution as G/WX, but the absolute [O] densities are much
 711 larger for both equinoxes and solstices. This is primarily because of the weakening of equa-
 712 torward circulation cells below 120 km, during both solstices and equinoxes. To zeroth

order, these circulation cells can be viewed as a ‘large-scale eddy’ mixing the thermosphere, thereby decreasing light species concentration (i.e., O) and increasing heavy species concentration (i.e., N₂), almost equally throughout the year, resulting in minimal effect on the SAO amplitude and phase. In Figure 6, the parameters were normalized, leading to an overall decrease of the SAO amplitude in G/NUDGE due to the contribution of the residual circulation as discussed previously. In contrast with Figures 8c and 8d, the WACCM-X model in Figure 8e exhibits stronger winter maxima. However, similar to both G/WX and G/NUDGE simulations, the summer-winter gradient is low. [O] from MSIS is shown here for consistency. We do not expect MSIS to have the correct distribution at these altitudes because of lack of [O] observations. It shows deep summer minima at mid-high latitudes that cancels out the winter maxima of the opposite hemisphere, resulting in equinoctial peaks in the global means.

Figure 9 shows neutral density at ~400 km (resembles major species, [O] at 400 km) from all our model simulations, as well as CHAMP and GRACE observations. The high latitude winter maxima observed for [O] at ~150 km has transitioned to high latitude summer maxima at ~400 km in this figure. This is because above ~300-400 km, the effect of larger summer temperatures dominates over that of compositional changes (due to thermospheric spoon mechanism) at a constant altitude (J. Emmert, 2015). The ρ for G/WX and G/NUDGE have the correct annual oscillation at high latitudes, however, the maxima at lower latitudes is at solstices, similar to [O] at ~150 km. Thus, the intra-annual variation in [O] stays the same at lower latitudes above ~150 km. The latitudinal distribution of G/NOSAO and G/MSIS agrees with MSIS, CHAMP and GRACE data, with slight phase differences. Comparing the absolute values of [O] and ρ in the Figures 8 and 9, it should be noted that the difference amongst the various GITM simulations is largest during solstices. Thus, major phase differences between the global means of the simulations in Figure 6, arise because of a relative increase in low latitude [O] during solstices in the lower thermospheric altitude region in G/WX and G/NUDGE.

Note that the results in a previous study by Malhotra et al. (2020) showed that using high summer [O] from WACCM-X at the lower boundary improves the O/N₂ agreement of GITM with the GUVI data during January and June. The WACCM-X driven GITM simulation showed a decreased O/N₂ gradient between the two hemispheres. We observe similar results in this study in Figure 8. However, since that study covered only a small number of days around the solstices, the wrong phase of global mean T-I SAO was not inferred. This raises the question, if WACCM-X represents the MLT state more accurately, how and why does the phase of T-I SAO in G/WX and G/NUDGE does not agree with observations? What are the additional processes in the lower thermosphere that are required to correct this discrepancy? We will henceforth look at the differences between the simulations during June solstice, when they are the largest.

3.6 June solstice

The panels on the left in Figure 10 show the averaged latitude-height distribution for temperature, whereas the panels on the right show the latitudinal gradient in temperature, for GITM simulations and WACCM-X around June solstice. Positive temperature gradient signifies larger temperature towards north (summer) and vice-versa. We show only G/MSIS and G/WX simulations here because G/MSIS shows a similar distribution as the G/NOSAO, and G/NUDGE is similar to WACCM-X. Overall, thermospheric temperature is larger in GITM than in WACCM-X. In the lower thermosphere, between 100-120 km, GITM shows low temperatures at high latitudes. This is because of the divergence and adiabatic cooling due to equatorward circulation cells shown in Figure 4.

Above 140 km, WACCM-X has the weakest temperature gradient between the two hemispheres. It shows positive temperature gradient at all heights. GITM on the other

764 hand shows a large positive gradient in both the hemispheres. As compared to G/MSIS,
 765 the gradient is slightly lower at equatorial latitudes in G/WX. A possible explanation
 766 for this difference was discussed by Malhotra et al. (2020). As discussed in that study,
 767 high summer [O] from WACCM-X at the lower boundary of GITM changes the wind mag-
 768 nitudes between 100-120 km. This high summer [O] leads to larger equatorward winds
 769 because of relatively larger equatorward-directed force, resulting in more adiabatic cool-
 770 ing. Similarly, lower winter [O] produces relatively slower equatorward winds resulting
 771 in less adiabatic cooling. This effect introduced near the lower boundary of the model
 772 has implications on the temperature structure of the whole thermosphere, resulting in
 773 the lowering of the summer temperature and relative increase in the winter temperature,
 774 thereby reducing the summer-to-winter gradient. These differences in gradients have a
 775 direct implication on the meridional and vertical winds, as the effectiveness of the ther-
 776 mospheric spoon mechanism depends on the temperature gradient between the two hemi-
 777 spheres (Jones Jr., Emmert, et al., 2018).

778 Figure 11 and Figure 4 demonstrate the variation in global meridional winds with
 779 altitude for different GITM simulations, HWM, and WACCM-X. Negative (positive) val-
 780 ues imply southward (northward) winds. Depending on the altitude, the difference in
 781 wind profiles in this figure arise because of the differences in wind patterns and the global
 782 mean magnitudes. At ~ 160 km, when all the model runs have summer-to-winter directed
 783 winds, the GITM simulations have weaker wind magnitudes as compared to HWM and
 784 WACCM-X. G/MSIS has stronger meridional winds than G/WX because of a larger tem-
 785 perature gradient at equatorial latitudes. For G/NUDGE (Figure 4), at this altitude,
 786 equatorward winds are observed, with stronger winds from summer high-latitudes to-
 787 wards equator. These winds change to summer-to-winter interhemispheric winds at about
 788 170 km, and maintain their lower amplitude relative to other simulations. WACCM-X
 789 shows larger summer-to-winter winds compared to all model runs despite the smaller tem-
 790 perature gradient. It is possible that the momentum sources from sub-grid processes, e.g.
 791 breaking gravity waves at ~ 140 km increase the magnitude of interhemispheric winds
 792 in WACCM-X. Another possible reason for weaker GITM winds might be stronger ion
 793 drag and viscosity. Note the momentum terms that contribute to GITM meridional winds
 794 were shown in Figure 4 of Malhotra et al. (2020). They showed that WACCM-X driven
 795 GITM had smaller winter-directed pressure gradient force at low latitudes, similar to the
 796 results shown in Figure 10. In the next section, we analyze the transport terms that con-
 797 tribute to the distribution of [O] in the lower thermosphere and provide evidence that
 798 low latitude accumulation in G/WX and G/NUDGE simulations are linked to weaker
 799 interhemispheric winds and mixing via the thermospheric spoon mechanism in GITM.

800 4 Discussion

801 The continuity equation in the vertical direction in GITM can be written as,

$$\frac{\partial \mathcal{N}_s}{\partial t} = -\frac{\partial u_{r,s}^{*(a)}}{\partial r} - \frac{2u_r^{*(b)}}{r} - u_{r,s} \frac{\partial \mathcal{N}_s^{*(c)}}{\partial r} + \frac{1}{N_s} \mathcal{S}_s^{*(d)} \quad (6)$$

802 where

$$\mathcal{N}_s = \ln(N_s) \quad (7)$$

803 Following the notation from Ridley et al. (2006), r is the radial distance measured from
 804 the center of the Earth. The subscript r denotes the component in the radial direction.
 805 $u_{r,s}$ is the vertical velocity of species s . N_s is the number density of species s . The source
 806 term \mathcal{S}_s for the species s includes the eddy diffusion and chemical sources and losses. Terms
 807 $^{*(a)}$ and $^{*(b)}$ signify the divergence of the vertical velocity and term $^{*(c)}$ represents the
 808 vertical advection. Here, we demonstrate these terms only for [O]. For the vertical con-
 809 tinuity equation, we show the sum of terms $^{*(a)}$, $^{*(b)}$ and $^{*(c)}$. These terms collectively
 810 are referred to as the transport terms. Amongst the source terms, the eddy diffusion terms

811 has negligible effect above 120 km. Eddy diffusion acts on the thermospheric densities
 812 primarily at ~ 100 km, but the effect is much smaller than the transport terms. The chem-
 813 ical source term for [O] shows equinoctial peaks and thus does not provide an explana-
 814 tion for the opposite SAO in G/WX and G/NUDGE. This is because of larger chem-
 815 ical loss of [O] during solstices in G/WX and G/NUDGE simulations relative to other
 816 simulations and is shown in the supporting information.

817 The continuity equation in the horizontal direction is :

$$\frac{\partial N_s}{\partial t} = -N_s \left(\frac{1}{r} \frac{\partial u_\theta}{\partial \theta} + \frac{1}{r \cos \theta} \frac{\partial u_\phi}{\partial \phi} - \frac{u_\theta \tan \theta}{r} \right)^{*(e)} - \left(\frac{u_\theta}{r} \frac{\partial N_s}{\partial \theta} + \frac{u_\phi}{r \cos \theta} \frac{\partial N_s}{\partial \phi} \right)^{*(f)}, \quad (8)$$

818 where, θ is latitude, ϕ is longitude, and the subscripts θ , ϕ denote the components in the
 819 respective directions. The first grouping on the right, labeled $^{*(e)}$, is the divergence term,
 820 while the second, labeled $^{*(f)}$, is the horizontal advection term. These are added together
 821 and considered as the horizontal transport terms below.

822 Figure 12 shows the latitudinal distribution of the horizontal (top panels) and ver-
 823 tical transport (bottom panels) terms that contribute to the global distribution of [O]
 824 at ~ 150 km shown in Figure 8. The panels on the left show the terms for G/MSIS while
 825 panels on the right are for the G/NUDGE. We only show G/MSIS and G/NUDGE, as
 826 we expect similar inference for G/NOSAO and G/WX, respectively. The magnitudes are
 827 different for the vertical and horizontal terms because the vertical continuity equation
 828 uses \mathcal{N}_s as shown in equation 7. G/MSIS shows high [O] accumulation in the winter high
 829 latitudes via both horizontal and vertical transport. G/NUDGE shows weaker winter
 830 accumulation driven exclusively by vertical transport, i.e., upwelling in summer and down-
 831 welling in winter. Alternatively, the horizontal transport term shows an accumulation
 832 at lower latitudes during solstices. The equatorward winds and the resulting convergence
 833 in the altitude region of 140-170 km, in addition to the weaker interhemispheric merid-
 834 ional winds above 170 km play an important role in the accumulation of [O] at low-latitudes.
 835 The meridional wind difference between G/WX and G/MSIS shown in Figure 11 is not
 836 large enough to be solely responsible for the difference in horizontal transport shown here.
 837 Transport of [O] to low latitudes in G/WX and G/NUDGE is a consequence of a larger
 838 summer high-latitude [O] in WACCM-X accompanied by overall weaker meridional winds
 839 in GITM. G/MSIS does not have this accumulation because it already has larger winter
 840 high-latitude [O] in the MLT. It is likely that since, pure WACCM-X has larger merid-
 841 ional winds, it does not show equatorial accumulation of [O]. It was demonstrated by X. Liu
 842 et al. (2014) that horizontal transport similarly also affects the peak location of the win-
 843 ter Helium bulge.

844 Our results show that in GITM, when the SAO in global mean [O] in the MLT has
 845 solstitial maxima, the T-I SAO also has solstitial maxima. The low-latitude accumula-
 846 tion of [O] during solstices in G/WX further contributes to the increase in the SAO am-
 847 plitude with altitude. From Figure 7, it is clear that the maximum change in the SAO
 848 phase for GITM runs is ~ 30 days, which is not enough to bring a seasonal change in the
 849 global mean SAO of G/WX and G/NUDGE. For achieving the equinoctial maxima in
 850 the thermosphere (to match observations), either the MLT SAO should have equinoc-
 851 tial maxima (G/MSIS) or the global mixing in the lower thermosphere during solstices
 852 should be strong enough to decrease the [O] below its equinoctial values. G/MSIS has
 853 the right phase of the T-I SAO in the lower thermosphere because it already has larger
 854 global mean [O] at equinoxes at the lower boundary. The thermospheric spoon mech-
 855 anism is enough to lead to the correct phase in G/NOSAO, but of lower amplitude in
 856 O/N₂. Since, we assume that G/WX and G/NUDGE better represent the MLT dynam-
 857 ics (match with SABER observations), there should be additional mechanisms acting in
 858 the lower thermosphere (not included in GITM) that decrease the solstitial [O]. Note,
 859 we also interpret similar results for January solstice (not shown here). The major dif-
 860 ference between January and June is that the meridional wind magnitudes are much weaker
 861 for January relative to June.

862 It can be suggested that since WACCM-X has the right SAO phase and latitudi-
 863 nal distribution of [O] and ρ in the upper thermosphere, the nudging altitude in GITM
 864 should be increased to above 140 km where WACCM-X wind speeds increase to achieve
 865 the right phase of SAO. However, when compared with integrated O/N₂ from GUVI (which
 866 reflects the lower T-I state at ~ 140 km), WACCM-X has the wrong SAO phase (Fig-
 867 ure 6a). Yue et al. (2019) showed that GUVI data has an SAO in both [O] and O/N₂
 868 with equinoctial peaks, which are in phase between the lower (8.4×10^{-4} Pa) and up-
 869 per thermosphere (6.35×10^{-6} Pa). Similar results were also obtained by Yu et al. (2020).
 870 We estimate 8.4×10^{-4} Pa to be ~ 140 -160 km. Even though the phase of the SAO is
 871 correct in WACCM-X at 400 km, it is not until 200 km that the SAO completely transi-
 872 tions from solstitial maxima to equinoctial maxima. GITM on the other hand is un-
 873 able to correct this as it has lower meridional wind speeds. This suggests that there are
 874 mechanisms missing in both models that could be responsible for this phase transition
 875 of the SAO in [O]. Jones Jr. et al. (2017) noted that this phase transition in the global
 876 mean SAO in TIME-GCM occurs between ~ 90 -100 km. The amplitude of the SAO de-
 877 creases to a minimum at 90 km, which is similar to the low amplitude observed by SABER
 878 in Figure 2d. However, the transition altitude in TIME-GCM is much lower, as we still
 879 observe solstitial maxima in SABER [O] at 97 km. Considering the results by Yue et al.
 880 (2019) and Jones Jr. et al. (2017), in order to have the right phase of the SAO in inte-
 881 grated O/N₂ (and match with the GUVI observations), the global SAO should transi-
 882 tion to equinoctial maxima in the lower thermosphere below ~ 140 km. However, mech-
 883 anisms driving this transition are not well understood. Jones Jr. et al. (2017) also ob-
 884 served a similar phase reversal between 90-100 km in the advective flux divergence, which
 885 was represented by a combination of meridional and vertical mean transport. This pro-
 886 vides a hint that dynamics in the lower thermosphere might be driving this transition.

887 Given the results shown herein, we offer the following thoughts about certain pro-
 888 cesses that can improve the amplitude and phase of the SAO in T-I models such as GITM:

- 889 • We introduce a seasonal variation in K_{zz} at the GITM lower boundary as a possi-
 890 ble solution, i.e., similar to that used by Qian et al. (2009) in TIE-GCM. Even
 891 though seasonally varying K_{zz} decreases the O/N₂ at solstices and increases it dur-
 892 ing equinoxes, it is not enough to completely reverse the phase of the oppositely-
 893 phased SAO. We also ran a simulation using WACCM-X version 2.1 at the lower
 894 boundary of GITM and got similar results as G/WX shown in this study. The tem-
 895 poral variation of global mean O/N₂ and ρ at 400 km for both of these simula-
 896 tions are provided in the supporting information.
- 897 • HWM winds have relatively larger summer-to-winter interhemispheric winds in
 898 the lower thermosphere. Thus, the lower thermospheric meridional wind magni-
 899 tudes can be increased in GITM to be in better agreement with HWM. Addition-
 900 ally, Jones Jr., Emmert, et al. (2018) demonstrated that the thermospheric spoon
 901 mechanism is most effective in the altitude regime where the thermosphere is tran-
 902 sitioning from a fully mixed state to that of diffusively separated state. This can
 903 be achieved by reducing ion drag and/or viscosity in GITM, or nudging the merid-
 904 ional winds to HWM. The exact magnitude of winds in this region remains to be
 905 studied as more thermospheric wind observations are made over the next few decades.
 906 Larger meridional transport during solstices can potentially improve the global
 907 SAO phase and reduce the equatorial accumulation of [O] in G/WX and G/NUDGE.
- 908 • We also observe that winter-to-summer winds between ~ 100 -120 km are much larger
 909 in TIDI data than in HWM and WACCM-X. In our G/NUDGE simulation, we
 910 found that this circulation results in the lowering of global mean (normalized) O/N₂,
 911 [O], ρ during solstices. If this residual circulation in WACCM-X and GITM is more
 912 accurately represented such that the magnitude of the winds are in agreement with
 913 TIDI data, the solstitial maxima seen in the G/WX and G/NUDGE simulations
 914 could decrease significantly.

915 Thus, the correct lower boundary conditions for GITM should be SABER/WACCM-
 916 X-like [O], with additional mechanisms that represent the state of lower thermospheric
 917 dynamics more accurately.

918 5 Summary and Conclusions

919 The T-I SAO is a large intra-annual density (mass and plasma) variation with max-
 920 ima during equinoxes and minima during solstices. It is successfully reproduced in most
 921 global whole atmosphere models. However, T-I models need estimates of the MLT state
 922 via accurate specification of lower boundary conditions for producing the right ampli-
 923 tude and phase of T-I SAO. This is especially difficult as there are limited global sources
 924 to validate the winds, composition, and temperature in the MLT. It has recently been
 925 shown that lower atmospheric perturbations from gravity waves and tides can affect and
 926 improve (in some studies) the modeling of T-I SAO in the global T-I models. This study
 927 explores a possible approach to improving the amplitude and phase of T-I SAO in GITM.

928 Our results show that GITM successfully reproduces the T-I SAO from first prin-
 929 ciples when no SAO is present at the lower boundary, however with lower amplitude. This
 930 demonstrates that the SAO is primarily driven by the internal thermospheric horizon-
 931 tal and vertical transport. Using the densities and temperature from MSIS (NRLMSISE-
 932 00) and winds from HWM (HWM14) at the lower boundary improves the amplitude and
 933 phase of SAO, especially in the lower thermosphere. However, there are still some dis-
 934 agreements between models and data regarding its phase and amplitude. For example,
 935 summer densities are underestimated and winter densities are overestimated during sol-
 936 stices, and the phase of SAO in ρ at 400 km leads the observations, especially during June
 937 and September.

938 Another problem is that the lower boundary condition in [O] specified at ~ 100 km
 939 by NRLMSISE-00 does not match data in this region from SABER. The [O] from SABER
 940 (at 97-100 km) has larger densities at solstices and at summer mid-high latitudes, op-
 941 posite to that of MSIS. It was found that [O] from WACCM-X at ~ 100 km matches the
 942 data better and was then used as lower boundary condition in GITM. The seasonal and
 943 latitudinal variations of other parameters are similar between MSIS and WACCM-X in
 944 this altitude region. Using GITM driven by the opposite [O] distribution from WACCM-
 945 X (G/WX) corrects for the summer-winter gradient. However, it does not improve the
 946 SAO at higher altitudes, but rather leads to maxima around solstices, which is 180° out
 947 of phase with respect to the MSIS driven GITM (G/MSIS) and the T-I observations. This
 948 is especially interesting, since the pure WACCM-X model has the appropriate phase of
 949 the upper thermospheric SAO, when compared to data. Nudging the dynamics in GITM
 950 towards WACCM-X up to 140 km (G/NUDGE), reduces the amplitude of this oppositely-
 951 phased SAO, but does not completely correct it.

952 We find that the maximum change in the SAO phase in GITM between the lower
 953 boundary and the upper thermosphere is ~ 30 days, which is not enough to have a phase
 954 shift on a seasonal scale. We reveal that in G/WX and G/NUDGE simulations, the max-
 955 ima in global mean [O] during the solstices are a result of the weaker thermospheric spoon
 956 mixing in GITM as compared to WACCM-X. Larger [O] at summer high latitudes in the
 957 MLT lead to accumulation of [O] at lower latitudes in the thermosphere during solstices,
 958 which further increases the amplitude of the oppositely-phased SAO. G/MSIS is able to
 959 achieve the right phase of T-I because it starts with the equinoctial maxima in [O] at
 960 the lower boundary. For G/NUDGE, equatorward winds and the resulting convergence
 961 between 100-140 km also add to this accumulation of [O]. The pure WACCM-X model
 962 also has the wrong phase of the SAO in the lower thermosphere, as it transitions from
 963 solstitial maxima towards equinoctial maxima between the altitudes ranging from 100-
 964 200 km. Since, several studies have shown that the global mean [O] and O/N_2 in the lower
 965 thermosphere have equinoctial maxima, we suggest that the phase transition from sol-

966 stitial to equinoctial maxima in the global mean SAO should occur in the altitude re-
967 gion of ~ 100 -140 km.

968 Since the [O] distribution in WACCM-X matches SABER observations at 97-100
969 km, there should be additional mechanisms acting in the lower thermosphere that de-
970 crease solstitial densities and nudge the phase of SAO towards equinoctial maxima. These
971 could include stronger thermospheric spoon circulation, stronger lower thermospheric resid-
972 ual circulation during solstices, and a seasonal variation in K_{zz} . It is also possible that
973 sub-grid processes such as gravity wave breaking could act as a momentum source for
974 the meridional winds, enhancing the meridional transport during the solstices. The ex-
975 act mechanisms that drive the phase transition of the SAO in the lower thermosphere
976 are currently unknown and will be the subject of future studies.

977 Our results emphasize the importance of accurate representation of the MLT state
978 and dynamics in the lower thermosphere in T-I models for better modeling of T-I SAO,
979 and thus agree with the appraisal by Picone et al. (2013). We infer that the lower ther-
980 mospheric region between 100-150 km is a complex and important region, as this is where
981 the effect of the larger scale neutral dynamics is strongest. Finally, as new models and
982 datasets are introduced, it becomes crucial to validate them with the older models and
983 datasets; this can help in addressing the gaps in our knowledge of the physical mecha-
984 nisms in the T-I region.

985 Acknowledgments

986 This work was supported by NASA grant #80NSSC20K1581. M. Jones Jr. gratefully ac-
987 knowledges support from NASA Heliophysics Early Career Investigator (NNH18ZDA001N
988 -ECIP/18-ECIP.2-0018) and Theory, Modeling, and Simulations (19-HTMS19.2-0056)
989 Programs. High computing resources were provided through Pleiades supercomputer by
990 NASA Advanced Supercomputing (NAS) housed at NASA Ames Research Center and
991 through Cheyenne supercomputer (doi:10.5065/D6RX99HX) by NCAR's Computational
992 and Information Systems Laboratory sponsored by the National Science Foundation and
993 other agencies.

994 GITM Simulations used in this study are available at [https://doi.org/10.7302/](https://doi.org/10.7302/9gp8-kx76)
995 [9gp8-kx76](https://doi.org/10.7302/9gp8-kx76). The atomic oxygen used in this study is from SABER data Version 2.0 and
996 was downloaded from <http://saber.gats-inc.com/data.php>. The level 3 O/N₂ GUVI
997 data was downloaded from <http://guvitimed.jhuapl.edu/>. Level 3 vector data from
998 TIDI was downloaded from <http://download.hao.ucar.edu/archive/tidi/data/vec0307a/>.
999 GNSS data can be accessed through the Madrigal distributed data system, <http://millstonehill>
1000 [.haystack.mit.edu/](http://millstonehill), as provided to the community by the Massachusetts Institute of
1001 Technology under support from US National Science Foundation grant AGS-1952737.
1002 CHAMP and GRACE data were downloaded from <http://thermosphere.tudelft.nl/>.

1003 References

- 1004 Bartels, J. (1932). Terrestrial-magnetic activity and its relations to solar phe-
1005 nomena. *Terrestrial Magnetism and Atmospheric Electricity*, 37(1), 1-52.
1006 Retrieved from [https://agupubs.onlinelibrary.wiley.com/doi/abs/](https://agupubs.onlinelibrary.wiley.com/doi/abs/10.1029/TE037i001p00001)
1007 [10.1029/TE037i001p00001](https://agupubs.onlinelibrary.wiley.com/doi/abs/10.1029/TE037i001p00001) doi: 10.1029/TE037i001p00001
- 1008 Boller, B. R., & Stolov, H. L. (1970). Kelvin?helmholtz instability and the
1009 semiannual variation of geomagnetic activity. *Journal of Geophysical*
1010 *Research (1896-1977)*, 75(31), 6073-6084. Retrieved from [https://](https://agupubs.onlinelibrary.wiley.com/doi/abs/10.1029/JA075i031p06073)
1011 agupubs.onlinelibrary.wiley.com/doi/abs/10.1029/JA075i031p06073
1012 doi: 10.1029/JA075i031p06073
- 1013 Brasseur, G., & Solomon, S. (1984). *Aeronomy of the middle atmosphere*. D.Reidel,
1014 Dordrecht.

- 1015 Bruisma, S., Tamagnan, D., & Biancale, R. (2004). Atmospheric densities de-
 1016 rived from champ/star accelerometer observations. *Planetary and Space*
 1017 *Science*, *52*(4), 297-312. Retrieved from [https://www.sciencedirect.com/](https://www.sciencedirect.com/science/article/pii/S003206330300237X)
 1018 [science/article/pii/S003206330300237X](https://www.sciencedirect.com/science/article/pii/S003206330300237X) doi: [https://doi.org/10.1016/](https://doi.org/10.1016/j.pss.2003.11.004)
 1019 [j.pss.2003.11.004](https://doi.org/10.1016/j.pss.2003.11.004)
- 1020 Bruisma, S. L., & Forbes, J. M. (2008). Medium- to large-scale density variability
 1021 as observed by champ. *Space Weather*, *6*(8). Retrieved from [https://agupubs](https://agupubs.onlinelibrary.wiley.com/doi/abs/10.1029/2008SW000411)
 1022 [.onlinelibrary.wiley.com/doi/abs/10.1029/2008SW000411](https://agupubs.onlinelibrary.wiley.com/doi/abs/10.1029/2008SW000411) doi: 10.1029/
 1023 2008SW000411
- 1024 Burns, A. G., Solomon, S. C., Wang, W., Qian, L., Zhang, Y., Paxton, L. J., ...
 1025 Liu, H. L. (2015). Explaining solar cycle effects on composition as it relates to
 1026 the winter anomaly. *Journal of Geophysical Research: Space Physics*, *120*(7),
 1027 5890-5898. Retrieved from [https://agupubs.onlinelibrary.wiley.com/](https://agupubs.onlinelibrary.wiley.com/doi/abs/10.1002/2015JA021220)
 1028 [doi/abs/10.1002/2015JA021220](https://agupubs.onlinelibrary.wiley.com/doi/abs/10.1002/2015JA021220) doi: 10.1002/2015JA021220
- 1029 Burrage, M. D., Vincent, R. A., Mayr, H. G., Skinner, W. R., Arnold, N. F., &
 1030 Hays, P. B. (1996). Long-term variability in the equatorial middle atmosphere
 1031 zonal wind. *Journal of Geophysical Research: Atmospheres*, *101*(D8), 12847-
 1032 12854. Retrieved from [https://agupubs.onlinelibrary.wiley.com/doi/](https://agupubs.onlinelibrary.wiley.com/doi/abs/10.1029/96JD00575)
 1033 [abs/10.1029/96JD00575](https://agupubs.onlinelibrary.wiley.com/doi/abs/10.1029/96JD00575) doi: 10.1029/96JD00575
- 1034 Cageao, R., & Kerr, R. (1984). Global distribution of helium in the upper atmo-
 1035 sphere during solar minimum. *Planetary and Space Science*, *32*(12), 1523 -
 1036 1529. Retrieved from [http://www.sciencedirect.com/science/article/](http://www.sciencedirect.com/science/article/pii/0032063384900199)
 1037 [pii/0032063384900199](http://www.sciencedirect.com/science/article/pii/0032063384900199) doi: [https://doi.org/10.1016/0032-0633\(84\)90019-9](https://doi.org/10.1016/0032-0633(84)90019-9)
- 1038 Chamberlin, P. C., Woods, T. N., & Eparvier, F. G. (2008). Flare irradiance spec-
 1039 tral model (FISM): Flare component algorithms and results. *Space Weather*,
 1040 *6*(5). Retrieved from [https://agupubs.onlinelibrary.wiley.com/doi/abs/](https://agupubs.onlinelibrary.wiley.com/doi/abs/10.1029/2007SW000372)
 1041 [10.1029/2007SW000372](https://agupubs.onlinelibrary.wiley.com/doi/abs/10.1029/2007SW000372) doi: 10.1029/2007SW000372
- 1042 Christensen, A. B., Paxton, L. J., Avery, S., Craven, J., Crowley, G., Humm,
 1043 D. C., ... Zhang, Y. (2003). Initial observations with the Global Ultra-
 1044 violet Imager (GUVI) in the NASA TIMED satellite mission. *Journal of*
 1045 *Geophysical Research: Space Physics*, *108*(A12). Retrieved from [https://](https://agupubs.onlinelibrary.wiley.com/doi/abs/10.1029/2003JA009918)
 1046 agupubs.onlinelibrary.wiley.com/doi/abs/10.1029/2003JA009918 doi:
 1047 10.1029/2003JA009918
- 1048 Cook, G. (1967). The large semi-annual variation in exospheric density: A possible
 1049 explanation. *Planetary and Space Science*, *15*(4), 627 - 632. Retrieved from
 1050 <http://www.sciencedirect.com/science/article/pii/0032063367900360>
 1051 doi: [https://doi.org/10.1016/0032-0633\(67\)90036-0](https://doi.org/10.1016/0032-0633(67)90036-0)
- 1052 Cook, G., & Scott, D. W. (1966). Exospheric densities near solar minimum derived
 1053 from the orbit of echo 2. *Planetary and Space Science*, *14*(11), 1149 - 1165.
 1054 Retrieved from [http://www.sciencedirect.com/science/article/pii/](http://www.sciencedirect.com/science/article/pii/0032063366900298)
 1055 [0032063366900298](http://www.sciencedirect.com/science/article/pii/0032063366900298) doi: [https://doi.org/10.1016/0032-0633\(66\)90029-8](https://doi.org/10.1016/0032-0633(66)90029-8)
- 1056 Cook, G. E. (1969a). Semi-annual variation in density at a height of 90 km. *Na-*
 1057 *ture*, *222*, 969-971. Retrieved from <https://doi.org/10.1038/222969a0> doi:
 1058 10.1038/222969a0
- 1059 Cook, G. E. (1969b, January). The semi-annual variation in the upper atmosphere:
 1060 A review. *Annales de Geophysique*, *25*, 451-469.
- 1061 Drob, D. P., Emmert, J. T., Meriwether, J. W., Makela, J. J., Doornbos, E., Conde,
 1062 M., ... Klenzing, J. H. (2015). An update to the horizontal wind model
 1063 (hwm): The quiet time thermosphere. *Earth and Space Science*, *2*(7), 301-
 1064 319. Retrieved from [https://agupubs.onlinelibrary.wiley.com/doi/abs/](https://agupubs.onlinelibrary.wiley.com/doi/abs/10.1002/2014EA000089)
 1065 [10.1002/2014EA000089](https://agupubs.onlinelibrary.wiley.com/doi/abs/10.1002/2014EA000089) doi: <https://doi.org/10.1002/2014EA000089>
- 1066 Dunker, T., Hoppe, U.-P., Feng, W., Plane, J. M., & Marsh, D. R. (2015). Meso-
 1067 spheric temperatures and sodium properties measured with the alomar na lidar
 1068 compared with waccm. *Journal of Atmospheric and Solar-Terrestrial Physics*,
 1069 *127*, 111 - 119. Retrieved from <http://www.sciencedirect.com/science/>

- 1070 article/pii/S136468261500005X (Layered Phenomena in the Mesopause
1071 Region) doi: <https://doi.org/10.1016/j.jastp.2015.01.003>
- 1072 Emmert, J. (2015). Thermospheric mass density: A review. *Advances in Space*
1073 *Research*, 56(5), 773 - 824. Retrieved from [http://www.sciencedirect.com/](http://www.sciencedirect.com/science/article/pii/S0273117715003944)
1074 [science/article/pii/S0273117715003944](http://www.sciencedirect.com/science/article/pii/S0273117715003944) doi: [https://doi.org/10.1016/](https://doi.org/10.1016/j.asr.2015.05.038)
1075 [j.asr.2015.05.038](https://doi.org/10.1016/j.asr.2015.05.038)
- 1076 Emmert, J. T. (2009). A long-term data set of globally averaged thermospheric
1077 total mass density. *Journal of Geophysical Research: Space Physics*, 114(A6).
1078 Retrieved from [https://agupubs.onlinelibrary.wiley.com/doi/abs/](https://agupubs.onlinelibrary.wiley.com/doi/abs/10.1029/2009JA014102)
1079 [10.1029/2009JA014102](https://agupubs.onlinelibrary.wiley.com/doi/abs/10.1029/2009JA014102) doi: <https://doi.org/10.1029/2009JA014102>
- 1080 Emmert, J. T. (2015). Altitude and solar activity dependence of 1967?2005 ther-
1081 mospheric density trends derived from orbital drag. *Journal of Geophysical Re-*
1082 *search: Space Physics*, 120(4), 2940-2950. Retrieved from [https://agupubs](https://agupubs.onlinelibrary.wiley.com/doi/abs/10.1002/2015JA021047)
1083 [.onlinelibrary.wiley.com/doi/abs/10.1002/2015JA021047](https://agupubs.onlinelibrary.wiley.com/doi/abs/10.1002/2015JA021047) doi: [https://](https://doi.org/10.1002/2015JA021047)
1084 doi.org/10.1002/2015JA021047
- 1085 Emmert, J. T., Drob, D. P., Picone, J. M., Siskind, D. E., Jones Jr, M., Mlynczak,
1086 M. G., ... Yuan, T. (2020). Nrlmsis 2.0: A whole-atmosphere empirical
1087 model of temperature and neutral species densities. *Earth and Space Science*,
1088 e2020EA001321. Retrieved from [https://agupubs.onlinelibrary.wiley](https://agupubs.onlinelibrary.wiley.com/doi/abs/10.1029/2020EA001321)
1089 [.com/doi/abs/10.1029/2020EA001321](https://agupubs.onlinelibrary.wiley.com/doi/abs/10.1029/2020EA001321) (e2020EA001321 2020EA001321) doi:
1090 [10.1029/2020EA001321](https://doi.org/10.1029/2020EA001321)
- 1091 Emmert, J. T., McDonald, S. E., Drob, D. P., Meier, R. R., Lean, J. L., & Picone,
1092 J. M. (2014). Attribution of interminima changes in the global thermosphere
1093 and ionosphere. *Journal of Geophysical Research: Space Physics*, 119(8), 6657-
1094 6688. Retrieved from [https://agupubs.onlinelibrary.wiley.com/doi/abs/](https://agupubs.onlinelibrary.wiley.com/doi/abs/10.1002/2013JA019484)
1095 [10.1002/2013JA019484](https://agupubs.onlinelibrary.wiley.com/doi/abs/10.1002/2013JA019484) doi: <https://doi.org/10.1002/2013JA019484>
- 1096 Emmert, J. T., Picone, J. M., & Meier, R. R. (2008). Thermospheric global
1097 average density trends, 1967?2007, derived from orbits of 5000 near-earth
1098 objects. *Geophysical Research Letters*, 35(5). Retrieved from [https://](https://agupubs.onlinelibrary.wiley.com/doi/abs/10.1029/2007GL032809)
1099 agupubs.onlinelibrary.wiley.com/doi/abs/10.1029/2007GL032809 doi:
1100 [10.1029/2007GL032809](https://doi.org/10.1029/2007GL032809)
- 1101 Forbes, J. M., Bruinsma, S. L., Zhang, X., & Oberheide, J. (2009). Surface-
1102 exosphere coupling due to thermal tides. *Geophysical Research Letters*, 36(15).
1103 Retrieved from [https://agupubs.onlinelibrary.wiley.com/doi/abs/](https://agupubs.onlinelibrary.wiley.com/doi/abs/10.1029/2009GL038748)
1104 [10.1029/2009GL038748](https://agupubs.onlinelibrary.wiley.com/doi/abs/10.1029/2009GL038748) doi: [10.1029/2009GL038748](https://doi.org/10.1029/2009GL038748)
- 1105 Fuller-Rowell, T., Rees, D., Quegan, S., Moffett, R., Codrescu, M., & Millward, G.
1106 (1996). A coupled thermosphere-ionosphere model (ctim). *STEP Report*, 239.
- 1107 Fuller-Rowell, T. J. (1998). The thermospheric spoon: A mechanism for the semi-
1108 annual density variation. *Journal of Geophysical Research: Space Physics*,
1109 103(A3), 3951-3956. Retrieved from [https://agupubs.onlinelibrary.wiley](https://agupubs.onlinelibrary.wiley.com/doi/abs/10.1029/97JA03335)
1110 [.com/doi/abs/10.1029/97JA03335](https://agupubs.onlinelibrary.wiley.com/doi/abs/10.1029/97JA03335) doi: [10.1029/97JA03335](https://doi.org/10.1029/97JA03335)
- 1111 Fuller-Rowell, T. J., & Evans, D. S. (1987). Height-integrated Pedersen and Hall
1112 conductivity patterns inferred from the TIROS-NOAA satellite data. *Jour-*
1113 *nal of Geophysical Research: Space Physics*, 92(A7), 7606-7618. Retrieved
1114 from [https://agupubs.onlinelibrary.wiley.com/doi/abs/10.1029/](https://agupubs.onlinelibrary.wiley.com/doi/abs/10.1029/JA092iA07p07606)
1115 [JA092iA07p07606](https://agupubs.onlinelibrary.wiley.com/doi/abs/10.1029/JA092iA07p07606) doi: [10.1029/JA092iA07p07606](https://doi.org/10.1029/JA092iA07p07606)
- 1116 Garcia, R. R., Dunkerton, T. J., Lieberman, R. S., & Vincent, R. A. (1997). Clima-
1117 tology of the semiannual oscillation of the tropical middle atmosphere. *Journal*
1118 *of Geophysical Research: Atmospheres*, 102(D22), 26019-26032. Retrieved from
1119 <https://agupubs.onlinelibrary.wiley.com/doi/abs/10.1029/97JD00207>
1120 doi: [10.1029/97JD00207](https://doi.org/10.1029/97JD00207)
- 1121 Garcia, R. R., & Solomon, S. (1985). The effect of breaking gravity waves on the
1122 dynamics and chemical composition of the mesosphere and lower thermo-
1123 sphere. *Journal of Geophysical Research: Atmospheres*, 90(D2), 3850-3868.
1124 Retrieved from <https://agupubs.onlinelibrary.wiley.com/doi/abs/>

- 1125 10.1029/JD090iD02p03850 doi: 10.1029/JD090iD02p03850
- 1126 Grossmann, K. U., Kaufmann, M., & Gerstner, E. (2000). A global measurement
1127 of lower thermosphere atomic oxygen densities. *Geophysical Research Letters*,
1128 *27*(9), 1387-1390. Retrieved from [https://agupubs.onlinelibrary.wiley](https://agupubs.onlinelibrary.wiley.com/doi/abs/10.1029/2000GL003761)
1129 [.com/doi/abs/10.1029/2000GL003761](https://agupubs.onlinelibrary.wiley.com/doi/abs/10.1029/2000GL003761) doi: 10.1029/2000GL003761
- 1130 Groves, G. (1972). Annual and semi-annual zonal wind components and correspond-
1131 ing temperature and density variations, 60130 km. *Planetary and Space Sci-*
1132 *ence*, *20*(12), 2099 - 2112. Retrieved from [http://www.sciencedirect.com/](http://www.sciencedirect.com/science/article/pii/0032063372900669)
1133 [science/article/pii/0032063372900669](http://www.sciencedirect.com/science/article/pii/0032063372900669) doi: [https://doi.org/10.1016/0032-](https://doi.org/10.1016/0032-0633(72)90066-9)
1134 [0633\(72\)90066-9](https://doi.org/10.1016/0032-0633(72)90066-9)
- 1135 Hagan, M. E., Maute, A., & Roble, R. G. (2009). Tropospheric tidal effects on
1136 the middle and upper atmosphere. *Journal of Geophysical Research: Space*
1137 *Physics*, *114*(A1). Retrieved from [https://agupubs.onlinelibrary.wiley](https://agupubs.onlinelibrary.wiley.com/doi/abs/10.1029/2008JA013637)
1138 [.com/doi/abs/10.1029/2008JA013637](https://agupubs.onlinelibrary.wiley.com/doi/abs/10.1029/2008JA013637) doi: 10.1029/2008JA013637
- 1139 Hedin, A. E. (1983). A revised thermospheric model based on mass spectrom-
1140 eter and incoherent scatter data: Msis-83. *Journal of Geophysical Re-*
1141 *search: Space Physics*, *88*(A12), 10170-10188. Retrieved from [https://](https://agupubs.onlinelibrary.wiley.com/doi/abs/10.1029/JA088iA12p10170)
1142 agupubs.onlinelibrary.wiley.com/doi/abs/10.1029/JA088iA12p10170
1143 doi: 10.1029/JA088iA12p10170
- 1144 Hedin, A. E. (1987). Msis-86 thermospheric model. *Journal of Geophysical*
1145 *Research: Space Physics*, *92*(A5), 4649-4662. Retrieved from [https://](https://agupubs.onlinelibrary.wiley.com/doi/abs/10.1029/JA092iA05p04649)
1146 agupubs.onlinelibrary.wiley.com/doi/abs/10.1029/JA092iA05p04649
1147 doi: 10.1029/JA092iA05p04649
- 1148 Hedin, A. E. (1991). Extension of the msis thermosphere model into the middle and
1149 lower atmosphere. *Journal of Geophysical Research: Space Physics*, *96*(A2),
1150 1159-1172. Retrieved from [https://agupubs.onlinelibrary.wiley.com/](https://agupubs.onlinelibrary.wiley.com/doi/abs/10.1029/90JA02125)
1151 [doi/abs/10.1029/90JA02125](https://agupubs.onlinelibrary.wiley.com/doi/abs/10.1029/90JA02125) doi: 10.1029/90JA02125
- 1152 Hedin, A. E., Salah, J. E., Evans, J. V., Reber, C. A., Newton, G. P., Spencer,
1153 N. W., ... McClure, J. P. (1977). A global thermospheric model based on
1154 mass spectrometer and incoherent scatter data msis, 1. n2 density and tem-
1155 perature. *Journal of Geophysical Research (1896-1977)*, *82*(16), 2139-2147.
1156 Retrieved from [https://agupubs.onlinelibrary.wiley.com/doi/abs/](https://agupubs.onlinelibrary.wiley.com/doi/abs/10.1029/JA082i016p02139)
1157 [10.1029/JA082i016p02139](https://agupubs.onlinelibrary.wiley.com/doi/abs/10.1029/JA082i016p02139) doi: <https://doi.org/10.1029/JA082i016p02139>
- 1158 Hodges, R. R. (1969). Eddy diffusion coefficients due to instabilities in internal grav-
1159 ity waves. *Journal of Geophysical Research*, *74*(16), 4087-4090. Retrieved
1160 from [https://agupubs.onlinelibrary.wiley.com/doi/abs/10.1029/](https://agupubs.onlinelibrary.wiley.com/doi/abs/10.1029/JA074i016p04087)
1161 [JA074i016p04087](https://agupubs.onlinelibrary.wiley.com/doi/abs/10.1029/JA074i016p04087) doi: 10.1029/JA074i016p04087
- 1162 Holton, J. R. (1983, 10). The Influence of Gravity Wave Breaking on the
1163 General Circulation of the Middle Atmosphere. *Journal of the Atmo-*
1164 *spheric Sciences*, *40*(10), 2497-2507. Retrieved from [https://doi.org/](https://doi.org/10.1175/1520-0469(1983)040<2497:TIOGWB>2.0.CO;2)
1165 [10.1175/1520-0469\(1983\)040<2497:TIOGWB>2.0.CO;2](https://doi.org/10.1175/1520-0469(1983)040<2497:TIOGWB>2.0.CO;2) doi: 10.1175/
1166 [1520-0469\(1983\)040<2497:TIOGWB>2.0.CO;2](https://doi.org/10.1175/1520-0469(1983)040<2497:TIOGWB>2.0.CO;2)
- 1167 Huba, J. D., & Liu, H.-L. (2020). Global modeling of equatorial spread f with
1168 sami3/waccm-x. *Geophysical Research Letters*, *47*(14), e2020GL088258.
1169 Retrieved from [https://agupubs.onlinelibrary.wiley.com/doi/abs/](https://agupubs.onlinelibrary.wiley.com/doi/abs/10.1029/2020GL088258)
1170 [10.1029/2020GL088258](https://agupubs.onlinelibrary.wiley.com/doi/abs/10.1029/2020GL088258) (e2020GL088258 10.1029/2020GL088258) doi:
1171 <https://doi.org/10.1029/2020GL088258>
- 1172 Jacchia, L. G. (1965, January). Static Diffusion Models of the Upper Atmosphere
1173 with Empirical Temperature Profiles. *Smithsonian Contributions to Astro-*
1174 *physics*, *8*, 215.
- 1175 Jacchia, L. G. (1970, May). New Static Models of the Thermosphere and Exosphere
1176 with Empirical Temperature Profiles. *SAO Special Report*, *313*.
- 1177 Jacchia, L. G. (1971, May). Revised Static Models of the Thermosphere and Exo-
1178 sphere with Empirical Temperature Profiles. *SAO Special Report*, *332*.
- 1179 Jacchia, L. G. (1977, March). Thermospheric Temperature, Density, and Composi-

- 1180 tion: New Models. *SAO Special Report*, 375.
- 1181 Jacchia, L. G., Slowey, J. H., & Campbell, I. (1969). A study of the semi-annual
1182 density variation in the upper atmosphere from 1958 to 1966, based on satellite
1183 drag analysis. *Planetary and Space Science*, 17(1), 49 - 60. Retrieved from
1184 <http://www.sciencedirect.com/science/article/pii/0032063369901226>
1185 doi: [https://doi.org/10.1016/0032-0633\(69\)90122-6](https://doi.org/10.1016/0032-0633(69)90122-6)
- 1186 Jones Jr., M., Drob, D. P., Siskind, D. E., McCormack, J. P., Maute, A., McDon-
1187 ald, S. E., & Dymond, K. F. (2018). Evaluating different techniques for
1188 constraining lower atmospheric variability in an upper atmosphere general
1189 circulation model: A case study during the 2010 sudden stratospheric warm-
1190 ing. *Journal of Advances in Modeling Earth Systems*, 10(12), 3076-3102.
1191 Retrieved from [https://agupubs.onlinelibrary.wiley.com/doi/abs/](https://agupubs.onlinelibrary.wiley.com/doi/abs/10.1029/2018MS001440)
1192 [10.1029/2018MS001440](https://doi.org/10.1029/2018MS001440) doi: <https://doi.org/10.1029/2018MS001440>
- 1193 Jones Jr., M., Emmert, J. T., Drob, D. P., Picone, J. M., & Meier, R. R. (2018).
1194 Origins of the thermosphere-ionosphere semiannual oscillation: Refor-
1195 mulating the thermospheric spoon mechanism. *Journal of Geophysi-
1196 cal Research: Space Physics*, 123(1), 931-954. Retrieved from [https://](https://agupubs.onlinelibrary.wiley.com/doi/abs/10.1002/2017JA024861)
1197 agupubs.onlinelibrary.wiley.com/doi/abs/10.1002/2017JA024861 doi:
1198 [10.1002/2017JA024861](https://doi.org/10.1002/2017JA024861)
- 1199 Jones Jr., M., Emmert, J. T., Drob, D. P., & Siskind, D. E. (2017). Middle atmo-
1200 sphere dynamical sources of the semiannual oscillation in the thermosphere
1201 and ionosphere. *Geophysical Research Letters*, 44(1), 12-21. Retrieved
1202 from [https://agupubs.onlinelibrary.wiley.com/doi/abs/10.1002/](https://agupubs.onlinelibrary.wiley.com/doi/abs/10.1002/2016GL071741)
1203 [2016GL071741](https://doi.org/10.1002/2016GL071741) doi: [10.1002/2016GL071741](https://doi.org/10.1002/2016GL071741)
- 1204 Jones Jr., M., Forbes, J. M., & Hagan, M. E. (2014). Tidal-induced net transport
1205 effects on the oxygen distribution in the thermosphere. *Geophysical Research
1206 Letters*, 41(14), 5272-5279. Retrieved from [https://agupubs.onlinelibrary](https://agupubs.onlinelibrary.wiley.com/doi/abs/10.1002/2014GL060698)
1207 [.wiley.com/doi/abs/10.1002/2014GL060698](https://doi.org/10.1002/2014GL060698) doi: [https://doi.org/10.1002/](https://doi.org/10.1002/2014GL060698)
1208 [2014GL060698](https://doi.org/10.1002/2014GL060698)
- 1209 Jones Jr., M., Sutton, E. K., Emmert, J. T., Siskind, D. E., & Drob, D. P. (2021).
1210 On the effects of mesospheric and lower thermospheric oxygen chemistry on
1211 the thermosphere and ionosphere semiannual oscillation. *Journal of Geo-
1212 physical Research: Space Physics*, n/a(n/a), e2020JA028647. Retrieved
1213 from [https://agupubs.onlinelibrary.wiley.com/doi/abs/10.1029/](https://agupubs.onlinelibrary.wiley.com/doi/abs/10.1029/2020JA028647)
1214 [2020JA028647](https://doi.org/10.1029/2020JA028647) (e2020JA028647 2020JA028647) doi: [https://doi.org/10.1029/](https://doi.org/10.1029/2020JA028647)
1215 [2020JA028647](https://doi.org/10.1029/2020JA028647)
- 1216 King-Hele, D. G. (1966). Semi-annual Variation in Upper-atmosphere Density. *Na-
1217 ture*, 210(5040), 1032. Retrieved from <https://doi.org/10.1038/2101032a0>
1218 doi: [10.1038/2101032a0](https://doi.org/10.1038/2101032a0)
- 1219 King-Hele, D. G. (1967, December). Upper Atmosphere Density in 1966-67 : the
1220 Dominance of a Semi-annual Variation at Heights near 200 km. *Nature*,
1221 216(5118), 880. doi: [10.1038/216880a0](https://doi.org/10.1038/216880a0)
- 1222 King-Hele, D., & Kingston, J. (1968). Air density at heights near 190 km in
1223 1966?67, from the orbit of secor 6. *Planetary and Space Science*, 16(5), 675 -
1224 691. Retrieved from [http://www.sciencedirect.com/science/article/pii/](http://www.sciencedirect.com/science/article/pii/0032063368901062)
1225 [0032063368901062](https://doi.org/10.1016/0032-0633(68)90106-2) doi: [https://doi.org/10.1016/0032-0633\(68\)90106-2](https://doi.org/10.1016/0032-0633(68)90106-2)
- 1226 King-Hele, D., & Walker, D. M. (1969). Revised profiles of air density at heights
1227 of 130?180 km, from the orbits of 1968-59a and b. *Planetary and Space Sci-
1228 ence*, 17(12), 2027 - 2029. Retrieved from [http://www.sciencedirect.com/](http://www.sciencedirect.com/science/article/pii/003206336990141X)
1229 [science/article/pii/003206336990141X](https://doi.org/10.1016/0032-0633(69)90141-X) doi: [https://doi.org/10.1016/](https://doi.org/10.1016/0032-0633(69)90141-X)
1230 [0032-0633\(69\)90141-X](https://doi.org/10.1016/0032-0633(69)90141-X)
- 1231 Lei, J., Matsuo, T., Dou, X., Sutton, E., & Luan, X. (2012). Annual and semi-
1232 annual variations of thermospheric density: Eof analysis of champ and grace
1233 data. *Journal of Geophysical Research: Space Physics*, 117(A1). Retrieved
1234 from <https://agupubs.onlinelibrary.wiley.com/doi/abs/10.1029/>

- 1235 2011JA017324 doi: <https://doi.org/10.1029/2011JA017324>
- 1236 Lin, S.-J. (2004). A vertically lagrangian finite-volume dynamical core for global
1237 models. *Monthly Weather Review*, *132*(10), 2293-2307. Retrieved from
1238 [https://doi.org/10.1175/1520-0493\(2004\)132<2293:AVLFDC>2.0.CO;2](https://doi.org/10.1175/1520-0493(2004)132<2293:AVLFDC>2.0.CO;2)
1239 doi: 10.1175/1520-0493(2004)132<2293:AVLFDC>2.0.CO;2
- 1240 Lindzen, R. S. (1981). Turbulence and stress owing to gravity wave and tidal
1241 breakdown. *Journal of Geophysical Research: Oceans*, *86*(C10), 9707-9714.
1242 Retrieved from [https://agupubs.onlinelibrary.wiley.com/doi/abs/](https://agupubs.onlinelibrary.wiley.com/doi/abs/10.1029/JC086iC10p09707)
1243 [10.1029/JC086iC10p09707](https://doi.org/10.1029/JC086iC10p09707) doi: 10.1029/JC086iC10p09707
- 1244 Liu, H., Foster, B. T., Hagan, M. E., McInerney, J. M., Maute, A., Qian, L., ...
1245 Oberheide, J. (2010). Thermosphere extension of the Whole Atmosphere
1246 Community Climate Model. *Journal of Geophysical Research: Space Physics*,
1247 *115*(A12). Retrieved from [https://agupubs.onlinelibrary.wiley.com/](https://agupubs.onlinelibrary.wiley.com/doi/abs/10.1029/2010JA015586)
1248 [doi/abs/10.1029/2010JA015586](https://doi.org/10.1029/2010JA015586) doi: 10.1029/2010JA015586
- 1249 Liu, H.-L., Bardeen, C. G., Foster, B. T., Lauritzen, P., Liu, J., Lu, G., ... Wang,
1250 W. (2018). Development and validation of the Whole Atmosphere Community
1251 Climate Model With Thermosphere and Ionosphere Extension (WACCM-
1252 X 2.0). *Journal of Advances in Modeling Earth Systems*, *10*(2), 381-402.
1253 Retrieved from [https://agupubs.onlinelibrary.wiley.com/doi/abs/](https://agupubs.onlinelibrary.wiley.com/doi/abs/10.1002/2017MS001232)
1254 [10.1002/2017MS001232](https://doi.org/10.1002/2017MS001232) doi: 10.1002/2017MS001232
- 1255 Liu, J., Liu, H., Wang, W., Burns, A. G., Wu, Q., Gan, Q., ... Schreiner, W. S.
1256 (2018). First results from the ionospheric extension of waccm-x dur-
1257 ing the deep solar minimum year of 2008. *Journal of Geophysical Re-*
1258 *search: Space Physics*, *123*(2), 1534-1553. Retrieved from [https://](https://agupubs.onlinelibrary.wiley.com/doi/abs/10.1002/2017JA025010)
1259 [agupubs.onlinelibrary.wiley.com/doi/abs/10.1002/2017JA025010](https://doi.org/10.1002/2017JA025010) doi:
1260 <https://doi.org/10.1002/2017JA025010>
- 1261 Liu, X., Wang, W., Thayer, J. P., Burns, A., Sutton, E., Solomon, S. C., ... Lucas,
1262 G. (2014). The winter helium bulge revisited. *Geophysical Research Letters*,
1263 *41*(19), 6603-6609. Retrieved from [https://agupubs.onlinelibrary.wiley](https://agupubs.onlinelibrary.wiley.com/doi/abs/10.1002/2014GL061471)
1264 [.com/doi/abs/10.1002/2014GL061471](https://doi.org/10.1002/2014GL061471) doi: 10.1002/2014GL061471
- 1265 Lühr, H., Rother, M., Khler, W., Ritter, P., & Grunwaldt, L. (2004). Ther-
1266 mospheric upwelling in the cusp region: Evidence from champ observa-
1267 tions. *Geophysical Research Letters*, *31*(6). Retrieved from [https://](https://agupubs.onlinelibrary.wiley.com/doi/abs/10.1029/2003GL019314)
1268 [agupubs.onlinelibrary.wiley.com/doi/abs/10.1029/2003GL019314](https://doi.org/10.1029/2003GL019314) doi:
1269 <https://doi.org/10.1029/2003GL019314>
- 1270 Malhotra, G., Ridley, A. J., Marsh, D. R., Wu, C., Paxton, L. J., & Mlynczak,
1271 M. G. (2020). Impacts of lower thermospheric atomic oxygen on thermospheric
1272 dynamics and composition using the global ionosphere thermosphere model.
1273 *Journal of Geophysical Research: Space Physics*, *125*(9), e2020JA027877.
1274 Retrieved from [https://agupubs.onlinelibrary.wiley.com/doi/abs/](https://agupubs.onlinelibrary.wiley.com/doi/abs/10.1029/2020JA027877)
1275 [10.1029/2020JA027877](https://doi.org/10.1029/2020JA027877) (e2020JA027877 10.1029/2020JA027877) doi:
1276 [10.1029/2020JA027877](https://doi.org/10.1029/2020JA027877)
- 1277 Malhotra, G., Ruohoniemi, J. M., Baker, J. B. H., Hibbins, R. E., & McWilliams,
1278 K. A. (2016). Hf radar observations of a quasi-biennial oscillation in mid-
1279 latitude mesospheric winds. *Journal of Geophysical Research: Atmospheres*,
1280 *121*(21), 12,677-12,689. Retrieved from [https://agupubs.onlinelibrary](https://agupubs.onlinelibrary.wiley.com/doi/abs/10.1002/2016JD024935)
1281 [.wiley.com/doi/abs/10.1002/2016JD024935](https://doi.org/10.1002/2016JD024935) doi: 10.1002/2016JD024935
- 1282 Maute, A., Hagan, M. E., Yudin, V., Liu, H.-L., & Yizengaw, E. (2015). Causes
1283 of the longitudinal differences in the equatorial vertical e b drift during
1284 the 2013 ssw period as simulated by the time-gcm. *Journal of Geophysi-*
1285 *cal Research: Space Physics*, *120*(6), 5117-5136. Retrieved from [https://](https://agupubs.onlinelibrary.wiley.com/doi/abs/10.1002/2015JA021126)
1286 [agupubs.onlinelibrary.wiley.com/doi/abs/10.1002/2015JA021126](https://doi.org/10.1002/2015JA021126) doi:
1287 <https://doi.org/10.1002/2015JA021126>
- 1288 Mayr, H. G., Harris, I., & Spencer, N. W. (1978). Some properties of upper at-
1289 mosphere dynamics. *Reviews of Geophysics*, *16*(4), 539-565. Retrieved

- 1290 from <https://agupubs.onlinelibrary.wiley.com/doi/abs/10.1029/RG016i004p00539> doi: 10.1029/RG016i004p00539
- 1291
- 1292 Mayr, H. G., & Volland, H. (1972). Theoretical model for the latitude dependence
- 1293 of the thermospheric annual and semiannual variations. *Journal of Geo-*
- 1294 *physical Research (1896-1977)*, 77(34), 6774-6790. Retrieved from [https://](https://agupubs.onlinelibrary.wiley.com/doi/abs/10.1029/JA077i034p06774)
- 1295 agupubs.onlinelibrary.wiley.com/doi/abs/10.1029/JA077i034p06774
- 1296 doi: <https://doi.org/10.1029/JA077i034p06774>
- 1297 McDonald, S. E., Sassi, F., & Mannucci, A. J. (2015). Sami3/sd-waccm-x simula-
- 1298 tions of ionospheric variability during northern winter 2009. *Space Weather*,
- 1299 13(9), 568-584. Retrieved from [https://agupubs.onlinelibrary.wiley](https://agupubs.onlinelibrary.wiley.com/doi/abs/10.1002/2015SW001223)
- 1300 [.com/doi/abs/10.1002/2015SW001223](https://agupubs.onlinelibrary.wiley.com/doi/abs/10.1002/2015SW001223) doi: [https://doi.org/10.1002/](https://doi.org/10.1002/2015SW001223)
- 1301 2015SW001223
- 1302 McLandress, C., Shepherd, G. G., Solheim, B. H., Burrage, M. D., Hays, P. B., &
- 1303 Skinner, W. R. (1996). Combined mesosphere/thermosphere winds using
- 1304 windii and hrDI data from the upper atmosphere research satellite. *Journal of*
- 1305 *Geophysical Research: Atmospheres*, 101(D6), 10441-10453. Retrieved from
- 1306 <https://agupubs.onlinelibrary.wiley.com/doi/abs/10.1029/95JD01706>
- 1307 doi: 10.1029/95JD01706
- 1308 Miyoshi, Y., Fujiwara, H., Jin, H., & Shinagawa, H. (2014). A global view of gravity
- 1309 waves in the thermosphere simulated by a general circulation model. *Jour-*
- 1310 *nal of Geophysical Research: Space Physics*, 119(7), 5807-5820. Retrieved
- 1311 from [https://agupubs.onlinelibrary.wiley.com/doi/abs/10.1002/](https://agupubs.onlinelibrary.wiley.com/doi/abs/10.1002/2014JA019848)
- 1312 2014JA019848 doi: 10.1002/2014JA019848
- 1313 Mlynczak, M. G. (1996). Energetics of the middle atmosphere: Theory and ob-
- 1314 servation requirements. *Advances in Space Research*, 17(11), 117 - 126.
- 1315 Retrieved from [http://www.sciencedirect.com/science/article/pii/](http://www.sciencedirect.com/science/article/pii/S0273117795007392)
- 1316 0273117795007392 doi: [https://doi.org/10.1016/0273-1177\(95\)00739-2](https://doi.org/10.1016/0273-1177(95)00739-2)
- 1317 Mlynczak, M. G. (1997). Energetics of the mesosphere and lower thermosphere
- 1318 and the SABER experiment. *Advances in Space Research*, 20(6), 1177 -
- 1319 1183. Retrieved from [http://www.sciencedirect.com/science/article/](http://www.sciencedirect.com/science/article/pii/S0273117797007692)
- 1320 [pii/S0273117797007692](http://www.sciencedirect.com/science/article/pii/S0273117797007692) (Coupling and Energetics in the Stratosphere-
- 1321 Mesosphere-Thermosphere- Ionosphere System) doi: [https://doi.org/10.1016/](https://doi.org/10.1016/S0273-1177(97)00769-2)
- 1322 S0273-1177(97)00769-2
- 1323 Mlynczak, M. G., Hunt, L. A., Mast, J. C., Thomas Marshall, B., Russell III,
- 1324 J. M., Smith, A. K., ... Gordley, L. L. (2013). Atomic oxygen in the
- 1325 mesosphere and lower thermosphere derived from SABER: Algorithm the-
- 1326 oretical basis and measurement uncertainty. *Journal of Geophysical Re-*
- 1327 *search: Atmospheres*, 118(11), 5724-5735. Retrieved from [https://](https://agupubs.onlinelibrary.wiley.com/doi/abs/10.1002/jgrd.50401)
- 1328 agupubs.onlinelibrary.wiley.com/doi/abs/10.1002/jgrd.50401 doi:
- 1329 10.1002/jgrd.50401
- 1330 Newell, R. E. (1966). Thermospheric energetics and a possible explanation of some
- 1331 observations of geomagnetic disturbances and radio aurorae. *Nature*, 211, 700-
- 1332 703. Retrieved from <https://doi.org/10.1038/211700a0> doi: 10.1038/
- 1333 211700a0
- 1334 Paetzold, H. K., & Zschörner, H. (1961). An annual and a semiannual variation of
- 1335 the upper air density. *Geofisica Pura e Applicata*, 48, 85-92. Retrieved from
- 1336 <https://doi.org/10.1007/BF01992371>
- 1337 Panka, P. A., Kutepov, A. A., Rezac, L., Kalogerakis, K. S., Feofilov, A. G., Marsh,
- 1338 D., ... Yi?it, E. (2018). Atomic oxygen retrieved from the saber 2.0- and
- 1339 1.6-?m radiances using new first-principles nighttime oh(v) model. *Geo-*
- 1340 *physical Research Letters*, 45(11), 5798-5803. Retrieved from [https://](https://agupubs.onlinelibrary.wiley.com/doi/abs/10.1029/2018GL077677)
- 1341 agupubs.onlinelibrary.wiley.com/doi/abs/10.1029/2018GL077677 doi:
- 1342 <https://doi.org/10.1029/2018GL077677>
- 1343 Paxton, L. J., Christensen, A. B., Humm, D. C., Ogorzalek, B. S., Pardoe, C. T.,
- 1344 Morrison, D., ... Meng, C.-I. (1999). Global Ultraviolet Imager (GUVI): mea-

- 1345 suring composition and energy inputs for the NASA Thermosphere Ionosphere
 1346 Mesosphere Energetics and Dynamics (TIMED) mission. In A. M. Larar
 1347 (Ed.), *Optical spectroscopic techniques and instrumentation for atmospheric*
 1348 *and space research iii* (Vol. 3756, pp. 265 – 276). SPIE. Retrieved from
 1349 <https://doi.org/10.1117/12.366380> doi: 10.1117/12.366380
- 1350 Picone, J. M., Hedin, A. E., Drob, D. P., & Aikin, A. C. (2002). Nrlmsise-00 em-
 1351 pirical model of the atmosphere: Statistical comparisons and scientific issues.
 1352 *Journal of Geophysical Research: Space Physics*, *107*(A12), SIA 15-1-SIA 15-
 1353 16. Retrieved from [https://agupubs.onlinelibrary.wiley.com/doi/abs/](https://agupubs.onlinelibrary.wiley.com/doi/abs/10.1029/2002JA009430)
 1354 [10.1029/2002JA009430](https://doi.org/10.1029/2002JA009430) doi: 10.1029/2002JA009430
- 1355 Picone, J. M., Meier, R. R., & Emmert, J. T. (2013). Theoretical tools for
 1356 studies of low-frequency thermospheric variability. *Journal of Geophysi-*
 1357 *cal Research: Space Physics*, *118*(9), 5853-5873. Retrieved from [https://](https://agupubs.onlinelibrary.wiley.com/doi/abs/10.1002/jgra.50472)
 1358 [agupubs.onlinelibrary.wiley.com/doi/abs/10.1002/jgra.50472](https://doi.org/10.1002/jgra.50472) doi:
 1359 [10.1002/jgra.50472](https://doi.org/10.1002/jgra.50472)
- 1360 Qian, L., Burns, A., & Yue, J. (2017). Evidence of the Lower Thermospheric
 1361 Winter-to-Summer circulation from SABER CO2 observations. *Geophys-*
 1362 *ical Research Letters*, *44*(20), 10,100-10,107. Retrieved from [https://](https://agupubs.onlinelibrary.wiley.com/doi/abs/10.1002/2017GL075643)
 1363 [agupubs.onlinelibrary.wiley.com/doi/abs/10.1002/2017GL075643](https://doi.org/10.1002/2017GL075643) doi:
 1364 [10.1002/2017GL075643](https://doi.org/10.1002/2017GL075643)
- 1365 Qian, L., Burns, A. G., Solomon, S. C., & Wang, W. (2013). Annual/semiannual
 1366 variation of the ionosphere. *Geophysical Research Letters*, *40*(10), 1928-1933.
 1367 Retrieved from [https://agupubs.onlinelibrary.wiley.com/doi/abs/](https://agupubs.onlinelibrary.wiley.com/doi/abs/10.1002/grl.50448)
 1368 [10.1002/grl.50448](https://doi.org/10.1002/grl.50448) doi: 10.1002/grl.50448
- 1369 Qian, L., Burns, A. G., Solomon, S. S., Smith, A. K., McInerney, J. M., Hunt,
 1370 L. A., ... Vitt, F. M. (2018). Temporal Variability of Atomic Hydrogen
 1371 From the Mesopause to the Upper Thermosphere. *Journal of Geophysi-*
 1372 *cal Research: Space Physics*, *123*(1), 1006-1017. Retrieved from [https://](https://agupubs.onlinelibrary.wiley.com/doi/abs/10.1002/2017JA024998)
 1373 [agupubs.onlinelibrary.wiley.com/doi/abs/10.1002/2017JA024998](https://doi.org/10.1002/2017JA024998) doi:
 1374 [10.1002/2017JA024998](https://doi.org/10.1002/2017JA024998)
- 1375 Qian, L., Solomon, S. C., & Kane, T. J. (2009). Seasonal variation of thermospheric
 1376 density and composition. *Journal of Geophysical Research: Space Physics*,
 1377 *114*(A1). Retrieved from [https://agupubs.onlinelibrary.wiley.com/doi/](https://agupubs.onlinelibrary.wiley.com/doi/abs/10.1029/2008JA013643)
 1378 [abs/10.1029/2008JA013643](https://doi.org/10.1029/2008JA013643) doi: 10.1029/2008JA013643
- 1379 Qian, L., & Yue, J. (2017). Impact of the lower thermospheric winter-to-summer
 1380 residual circulation on thermospheric composition. *Geophysical Research Let-*
 1381 *ters*, *44*(9), 3971-3979. Retrieved from [https://agupubs.onlinelibrary](https://agupubs.onlinelibrary.wiley.com/doi/abs/10.1002/2017GL073361)
 1382 [.wiley.com/doi/abs/10.1002/2017GL073361](https://doi.org/10.1002/2017GL073361) doi: 10.1002/2017GL073361
- 1383 Reigber, C., Lühr, H., & Schwintzer, P. (2002). Champ mission status. *Ad-*
 1384 *vances in Space Research*, *30*(2), 129-134. Retrieved from [https://](https://www.sciencedirect.com/science/article/pii/S0273117702002764)
 1385 [www.sciencedirect.com/science/article/pii/S0273117702002764](https://doi.org/10.1016/S0273-1177(02)00276-4) doi:
 1386 [https://doi.org/10.1016/S0273-1177\(02\)00276-4](https://doi.org/10.1016/S0273-1177(02)00276-4)
- 1387 Rezac, L., Jian, Y., Yue, J., Russell III, J. M., Kutepov, A., Garcia, R., ... Bernath,
 1388 P. (2015). Validation of the global distribution of CO2 volume mixing ratio in
 1389 the mesosphere and lower thermosphere from SABER. *Journal of Geophysical*
 1390 *Research: Atmospheres*, *120*(23), 12,067-12,081. Retrieved from [https://](https://agupubs.onlinelibrary.wiley.com/doi/abs/10.1002/2015JD023955)
 1391 [agupubs.onlinelibrary.wiley.com/doi/abs/10.1002/2015JD023955](https://doi.org/10.1002/2015JD023955) doi:
 1392 [10.1002/2015JD023955](https://doi.org/10.1002/2015JD023955)
- 1393 Richmond, A. D., Ridley, E. C., & Roble, R. G. (1992). A thermosphere/ionosphere
 1394 general circulation model with coupled electrodynamics. *Geophysical Research*
 1395 *Letters*, *19*(6), 601-604. Retrieved from [https://agupubs.onlinelibrary](https://agupubs.onlinelibrary.wiley.com/doi/abs/10.1029/92GL00401)
 1396 [.wiley.com/doi/abs/10.1029/92GL00401](https://doi.org/10.1029/92GL00401) doi: 10.1029/92GL00401
- 1397 Ridley, A., Deng, Y., & Tth, G. (2006). The global ionosphere thermosphere
 1398 model. *Journal of Atmospheric and Solar-Terrestrial Physics*, *68*(8), 839 -
 1399 864. Retrieved from [http://www.sciencedirect.com/science/article/pii/](http://www.sciencedirect.com/science/article/pii/S0273117706002764)

- 1400 S1364682606000071 doi: <https://doi.org/10.1016/j.jastp.2006.01.008>
- 1401 Rienecker, M. M., Suarez, M. J., Gelaro, R., Todling, R., Bacmeister, J., Liu, E.,
1402 ... Woollen, J. (2011). MERRA: NASA's modern-era retrospective anal-
1403 ysis for research and applications. *Journal of Climate*, 24(14), 3624-3648.
1404 Retrieved from <https://doi.org/10.1175/JCLI-D-11-00015.1> doi:
1405 10.1175/JCLI-D-11-00015.1
- 1406 Rishbeth, H. (2007). Thermospheric targets. *Eos, Transactions American Geophysi-
1407 cal Union*, 88(17), 189-193. Retrieved from [https://agupubs.onlinelibrary](https://agupubs.onlinelibrary.wiley.com/doi/abs/10.1029/2007EO170002)
1408 [.wiley.com/doi/abs/10.1029/2007EO170002](https://agupubs.onlinelibrary.wiley.com/doi/abs/10.1029/2007EO170002) doi: 10.1029/2007EO170002
- 1409 Rishbeth, H., & Mendillo, M. (2001). Patterns of f2-layer variability. *Journal of At-
1410 mospheric and Solar-Terrestrial Physics*, 63(15), 1661 - 1680. Retrieved from
1411 <http://www.sciencedirect.com/science/article/pii/S1364682601000360>
1412 doi: [https://doi.org/10.1016/S1364-6826\(01\)00036-0](https://doi.org/10.1016/S1364-6826(01)00036-0)
- 1413 Rishbeth, H., & Müller-Wodarg, I. C. F. (1999). Vertical circulation and thermo-
1414 spheric composition: a modelling study. *Annales Geophysicae*, 17(6), 794-805.
1415 Retrieved from <https://angeo.copernicus.org/articles/17/794/1999/>
1416 doi: 10.1007/s00585-999-0794-x
- 1417 Rishbeth, H., Sedgemore-Schulthess, K. J. F., & Ulich, T. (2000). Semiannual
1418 and annual variations in the height of the ionospheric f2-peak. *Annales Geo-
1419 physicae*, 18(3), 285-299. Retrieved from [https://angeo.copernicus.org/](https://angeo.copernicus.org/articles/18/285/2000/)
1420 [articles/18/285/2000/](https://angeo.copernicus.org/articles/18/285/2000/) doi: 10.1007/s00585-000-0285-6
- 1421 Russell, C. T., & McPherron, R. L. (1973). Semiannual variation of geomag-
1422 netic activity. *Journal of Geophysical Research (1896-1977)*, 78(1), 92-108.
1423 Retrieved from [https://agupubs.onlinelibrary.wiley.com/doi/abs/](https://agupubs.onlinelibrary.wiley.com/doi/abs/10.1029/JA078i001p00092)
1424 [10.1029/JA078i001p00092](https://agupubs.onlinelibrary.wiley.com/doi/abs/10.1029/JA078i001p00092) doi: 10.1029/JA078i001p00092
- 1425 Russell, J. P., Lowe, R., & Ward, W. (2004). Atomic oxygen annual and semi-annual
1426 variations in the mesopause region for mid and equatorial latitudes. *Journal of*
1427 *Atmospheric and Solar-Terrestrial Physics*, 66(6), 451 - 461. Retrieved from
1428 <http://www.sciencedirect.com/science/article/pii/S1364682604000124>
1429 (Dynamics and Chemistry of the MLT Region - PSMOS 2002 International
1430 Symposium) doi: <https://doi.org/10.1016/j.jastp.2004.01.004>
- 1431 Russell III, J., Mlynczak, M., Gordley, L., Tansock, J., & Esplin, R. (1999, 10).
1432 Overview of the SABER experiment and preliminary calibration results. *Pro-
1433 ceedings of SPIE - The International Society for Optical Engineering*, 3756.
- 1434 Salinas, C. C. J. H., Chang, L. C., Liang, M. ., Yue, J., Russell, J., & Mlynczak,
1435 M. (2016). Impacts of SABER CO2 based eddy diffusion coefficients in the
1436 lower thermosphere on the ionosphere/thermosphere. *Journal of Geophysical*
1437 *Research: Space Physics*, 121(12), 12,080-12,092. Retrieved from [https://](https://agupubs.onlinelibrary.wiley.com/doi/abs/10.1002/2016JA023161)
1438 agupubs.onlinelibrary.wiley.com/doi/abs/10.1002/2016JA023161 doi:
1439 10.1002/2016JA023161
- 1440 Sassi, F., Liu, H.-L., & Emmert, J. T. (2016). Traveling planetary-scale waves in the
1441 lower thermosphere: Effects on neutral density and composition during solar
1442 minimum conditions. *Journal of Geophysical Research: Space Physics*, 121(2),
1443 1780-1801. Retrieved from [https://agupubs.onlinelibrary.wiley.com/](https://agupubs.onlinelibrary.wiley.com/doi/abs/10.1002/2015JA022082)
1444 [doi/abs/10.1002/2015JA022082](https://agupubs.onlinelibrary.wiley.com/doi/abs/10.1002/2015JA022082) doi: 10.1002/2015JA022082
- 1445 Sheese, P. E., McDade, I. C., Gattinger, R. L., & Llewellyn, E. J. (2011). Atomic
1446 oxygen densities retrieved from Optical Spectrograph and Infrared Imaging
1447 System observations of O2 A-band airglow emission in the mesosphere and
1448 lower thermosphere. *Journal of Geophysical Research: Atmospheres*, 116(D1).
1449 Retrieved from [https://agupubs.onlinelibrary.wiley.com/doi/abs/](https://agupubs.onlinelibrary.wiley.com/doi/abs/10.1029/2010JD014640)
1450 [10.1029/2010JD014640](https://agupubs.onlinelibrary.wiley.com/doi/abs/10.1029/2010JD014640) doi: 10.1029/2010JD014640
- 1451 Siskind, D. E., Drob, D. P., Dymond, K. F., & McCormack, J. P. (2014). Simula-
1452 tions of the effects of vertical transport on the thermosphere and ionosphere
1453 using two coupled models. *Journal of Geophysical Research: Space Physics*,
1454 119(2), 1172-1185. Retrieved from [https://agupubs.onlinelibrary.wiley](https://agupubs.onlinelibrary.wiley.com/doi/abs/10.1029/2013JA019311)

- 1455 .com/doi/abs/10.1002/2013JA019116 doi: 10.1002/2013JA019116
- 1456 Smith, A. K., Harvey, V. L., Mlynczak, M. G., Funke, B., Garca-Comas, M., Hervig,
1457 M., ... Walker, K. A. (2013). Satellite observations of ozone in the upper
1458 mesosphere. *Journal of Geophysical Research: Atmospheres*, 118(11), 5803-
1459 5821. Retrieved from [https://agupubs.onlinelibrary.wiley.com/doi/abs/](https://agupubs.onlinelibrary.wiley.com/doi/abs/10.1002/jgrd.50445)
1460 [10.1002/jgrd.50445](https://agupubs.onlinelibrary.wiley.com/doi/abs/10.1002/jgrd.50445) doi: 10.1002/jgrd.50445
- 1461 Smith, A. K., Marsh, D. R., Mlynczak, M. G., & Mast, J. C. (2010). Temporal
1462 variations of atomic oxygen in the upper mesosphere from SABER. *Journal*
1463 *of Geophysical Research: Atmospheres*, 115(D18). Retrieved from [https://](https://agupubs.onlinelibrary.wiley.com/doi/abs/10.1029/2009JD013434)
1464 agupubs.onlinelibrary.wiley.com/doi/abs/10.1029/2009JD013434 doi:
1465 [10.1029/2009JD013434](https://doi.org/10.1029/2009JD013434)
- 1466 Strickland, D. J., Evans, J. S., & Paxton, L. J. (1995). Satellite remote sens-
1467 ing of thermospheric O₂ and solar EUV: 1. theory. *Journal of Geophys-*
1468 *ical Research: Space Physics*, 100(A7), 12217-12226. Retrieved from
1469 <https://agupubs.onlinelibrary.wiley.com/doi/abs/10.1029/95JA00574>
1470 doi: <https://doi.org/10.1029/95JA00574>
- 1471 Sutton, E. K. (2011). Accelerometer-derived atmospheric density from the CHAMP
1472 and GRACE satellites. *Tech. Memo., DTIC ADA537198, Air Force Res. Lab.,*
1473 *Kirtland AFB, N. M.* Retrieved from [https://apps.dtic.mil/sti/pdfs/](https://apps.dtic.mil/sti/pdfs/ADA537198.pdf)
1474 [ADA537198.pdf](https://apps.dtic.mil/sti/pdfs/ADA537198.pdf)
- 1475 Sutton, E. K. (2016). Interhemispheric transport of light neutral species in the ther-
1476 mosphere. *Geophysical Research Letters*, 43(24), 12,325-12,332. Retrieved
1477 from [https://agupubs.onlinelibrary.wiley.com/doi/abs/10.1002/](https://agupubs.onlinelibrary.wiley.com/doi/abs/10.1002/2016GL071679)
1478 [2016GL071679](https://agupubs.onlinelibrary.wiley.com/doi/abs/10.1002/2016GL071679) doi: 10.1002/2016GL071679
- 1479 Swenson, G., Yee, Y., Vargas, F., & Liu, A. (2018). Vertical diffusion trans-
1480 port of atomic oxygen in the mesopause region consistent with chemical
1481 losses and continuity: Global mean and inter-annual variability. *Journal of*
1482 *Atmospheric and Solar-Terrestrial Physics*, 178, 47 - 57. Retrieved from
1483 <http://www.sciencedirect.com/science/article/pii/S1364682617305552>
1484 doi: <https://doi.org/10.1016/j.jastp.2018.05.014>
- 1485 Swenson, G. R., Salinas, C. C. J. H., Vargas, F., Zhu, Y., Kaufmann, M., Jones Jr.,
1486 M., ... Yee, J. H. (2019). Determination of global mean eddy diffu-
1487 sive transport in the mesosphere and lower thermosphere from atomic
1488 oxygen and carbon dioxide climatologies. *Journal of Geophysical Re-*
1489 *search: Atmospheres*, 124(23), 13519-13533. Retrieved from [https://](https://agupubs.onlinelibrary.wiley.com/doi/abs/10.1029/2019JD031329)
1490 agupubs.onlinelibrary.wiley.com/doi/abs/10.1029/2019JD031329 doi:
1491 <https://doi.org/10.1029/2019JD031329>
- 1492 Tapley, B. D., Bettapur, S., Watkins, M., & Reigber, C. (2004). The gravity re-
1493 covery and climate experiment: Mission overview and early results. *Geophys-*
1494 *ical Research Letters*, 31(9). Retrieved from [https://agupubs.onlinelibrary](https://agupubs.onlinelibrary.wiley.com/doi/abs/10.1029/2004GL019920)
1495 [.wiley.com/doi/abs/10.1029/2004GL019920](https://agupubs.onlinelibrary.wiley.com/doi/abs/10.1029/2004GL019920) doi: [https://doi.org/10.1029/](https://doi.org/10.1029/2004GL019920)
1496 [2004GL019920](https://doi.org/10.1029/2004GL019920)
- 1497 Vierinen, J., Coster, A. J., Rideout, W. C., Erickson, P. J., & Norberg, J. (2016).
1498 Statistical framework for estimating GNSS bias. *Atmospheric Measurement*
1499 *Techniques*, 9(3), 1303-1312. Retrieved from [https://amt.copernicus.org/](https://amt.copernicus.org/articles/9/1303/2016/)
1500 [articles/9/1303/2016/](https://amt.copernicus.org/articles/9/1303/2016/) doi: 10.5194/amt-9-1303-2016
- 1501 Volland, H., Wulf-Mathies, C., & Priester, W. (1972). On the annual and
1502 semiannual variations of the thermospheric density. *Journal of Atmo-*
1503 *spheric and Terrestrial Physics*, 34(6), 1053 - 1063. Retrieved from
1504 <http://www.sciencedirect.com/science/article/pii/0021916972900943>
1505 doi: [https://doi.org/10.1016/0021-9169\(72\)90094-3](https://doi.org/10.1016/0021-9169(72)90094-3)
- 1506 Walterscheid, R. L. (1982). The semiannual oscillation in the thermosphere as a
1507 conduction mode. *Journal of Geophysical Research: Space Physics*, 87(A12),
1508 10527-10535. Retrieved from [https://agupubs.onlinelibrary.wiley.com/](https://agupubs.onlinelibrary.wiley.com/doi/abs/10.1029/JA087iA12p10527)
1509 [doi/abs/10.1029/JA087iA12p10527](https://agupubs.onlinelibrary.wiley.com/doi/abs/10.1029/JA087iA12p10527) doi: 10.1029/JA087iA12p10527

- 1510 Wang, J. C., Chang, L. C., Yue, J., Wang, W., & Siskind, D. E. (2017). The quasi
1511 2 day wave response in time-gcm nudged with nogaps-alpha. *Journal of Geo-*
1512 *physical Research: Space Physics*, *122*(5), 5709-5732. Retrieved from [https://](https://agupubs.onlinelibrary.wiley.com/doi/abs/10.1002/2016JA023745)
1513 agupubs.onlinelibrary.wiley.com/doi/abs/10.1002/2016JA023745 doi:
1514 <https://doi.org/10.1002/2016JA023745>
- 1515 Weimer, D. R. (2005). Improved ionospheric electrodynamic models and applica-
1516 tion to calculating joule heating rates. *Journal of Geophysical Research: Space*
1517 *Physics*, *110*(A5). Retrieved from [https://agupubs.onlinelibrary.wiley](https://agupubs.onlinelibrary.wiley.com/doi/abs/10.1029/2004JA010884)
1518 [.com/doi/abs/10.1029/2004JA010884](https://agupubs.onlinelibrary.wiley.com/doi/abs/10.1029/2004JA010884) doi: 10.1029/2004JA010884
- 1519 Wu, Q., Schreiner, W. S., Ho, S.-P., Liu, H.-L., & Qian, L. (2017). Observations
1520 and simulations of eddy diffusion and tidal effects on the semiannual oscillation
1521 in the ionosphere. *Journal of Geophysical Research: Space Physics*, *122*(10),
1522 10,502-10,510. Retrieved from [https://agupubs.onlinelibrary.wiley.com/](https://agupubs.onlinelibrary.wiley.com/doi/abs/10.1002/2017JA024341)
1523 [doi/abs/10.1002/2017JA024341](https://agupubs.onlinelibrary.wiley.com/doi/abs/10.1002/2017JA024341) doi: 10.1002/2017JA024341
- 1524 Yee, J. H. (2003). TIMED mission science overview. *John Hopkins APL Technical*
1525 *Digest*, *24*(2), 136-141 Apr-Jun.
- 1526 Yu, T., Ren, Z., Yu, Y., Yue, X., Zhou, X., & Wan, W. (2020). Compari-
1527 son of reference heights of O/N2 and \sum O/N2 based on GUVI dayside
1528 limb measurement. *Space Weather*, *18*(1), e2019SW002391. Retrieved
1529 from [https://agupubs.onlinelibrary.wiley.com/doi/abs/10.1029/](https://agupubs.onlinelibrary.wiley.com/doi/abs/10.1029/2019SW002391)
1530 [2019SW002391](https://agupubs.onlinelibrary.wiley.com/doi/abs/10.1029/2019SW002391) (e2019SW002391 2019SW002391) doi: [https://doi.org/](https://doi.org/10.1029/2019SW002391)
1531 [10.1029/2019SW002391](https://doi.org/10.1029/2019SW002391)
- 1532 Yue, J., Jian, Y., Wang, W., Meier, R., Burns, A., Qian, L., ... Mlynczak, M.
1533 (2019). Annual and Semiannual Oscillations of Thermospheric Compo-
1534 sition in TIMED/GUVI Limb measurements. *Journal of Geophysical*
1535 *Research: Space Physics*, *124*(4), 3067-3082. Retrieved from [https://](https://agupubs.onlinelibrary.wiley.com/doi/abs/10.1029/2019JA026544)
1536 agupubs.onlinelibrary.wiley.com/doi/abs/10.1029/2019JA026544 doi:
1537 [10.1029/2019JA026544](https://doi.org/10.1029/2019JA026544)
- 1538 Zhang, S. P., McLandress, C., & Shepherd, G. G. (2007). Satellite observa-
1539 tions of mean winds and tides in the lower thermosphere: 2. wind imag-
1540 ing interferometer monthly winds for 1992 and 1993. *Journal of Geo-*
1541 *physical Research: Atmospheres*, *112*(D21). Retrieved from [https://](https://agupubs.onlinelibrary.wiley.com/doi/abs/10.1029/2007JD008457)
1542 agupubs.onlinelibrary.wiley.com/doi/abs/10.1029/2007JD008457 doi:
1543 [10.1029/2007JD008457](https://doi.org/10.1029/2007JD008457)

Table 1. GITM Runs

Simulation	Density Lower Boundary Condition	Winds Lower Boundary Condition
G/MSIS	MSIS	HWM
G/NOSAO	MSIS with AO and SAO set to 0	0
G/WX	WACCM-X	WACCM-X
G/NUDGE	WACCM-X	Nudged to WACCM-X till 140 km

Model Run	ρ at 400 km		O/N ₂		TEC	
	SAO Amplitude (%)	SAO Phase	SAO Amplitude (%)	SAO Phase	SAO Amplitude (%)	SAO Phase
G/NOSAO	18.2	82	3.9	84	12.9	81
G/MSIS	16.6	83	9.6	95	21.0	87
G/WX	18.9	34	23.1	16	25.2	22
G/NUDGE	14.9	38	12.9	19	12.2	46
WACCM-X	10.0	76	4.2	14	9.4	70
MSIS	17.5	104	9.3	100		
GRACE	16.2	97				
CHAMP	17.3	101				
Emmert Dataset	25.6	97				
GUVI			18.2	89		
GNSS					12.9	95
TIE-GCM, w/ Q09	16.2	122			26.5	129
TIME-GCM Standard	12.8	114			19.7	106

Table 2. SAO Amplitude and Phase for different model runs and observations. The amplitude is determined by fitting a least squares semiannual variation to the data. Phase is the day of first maxima. TIE-GCM and TIME-GCM values are from Jones Jr. et al. (2017).

Author Manuscript

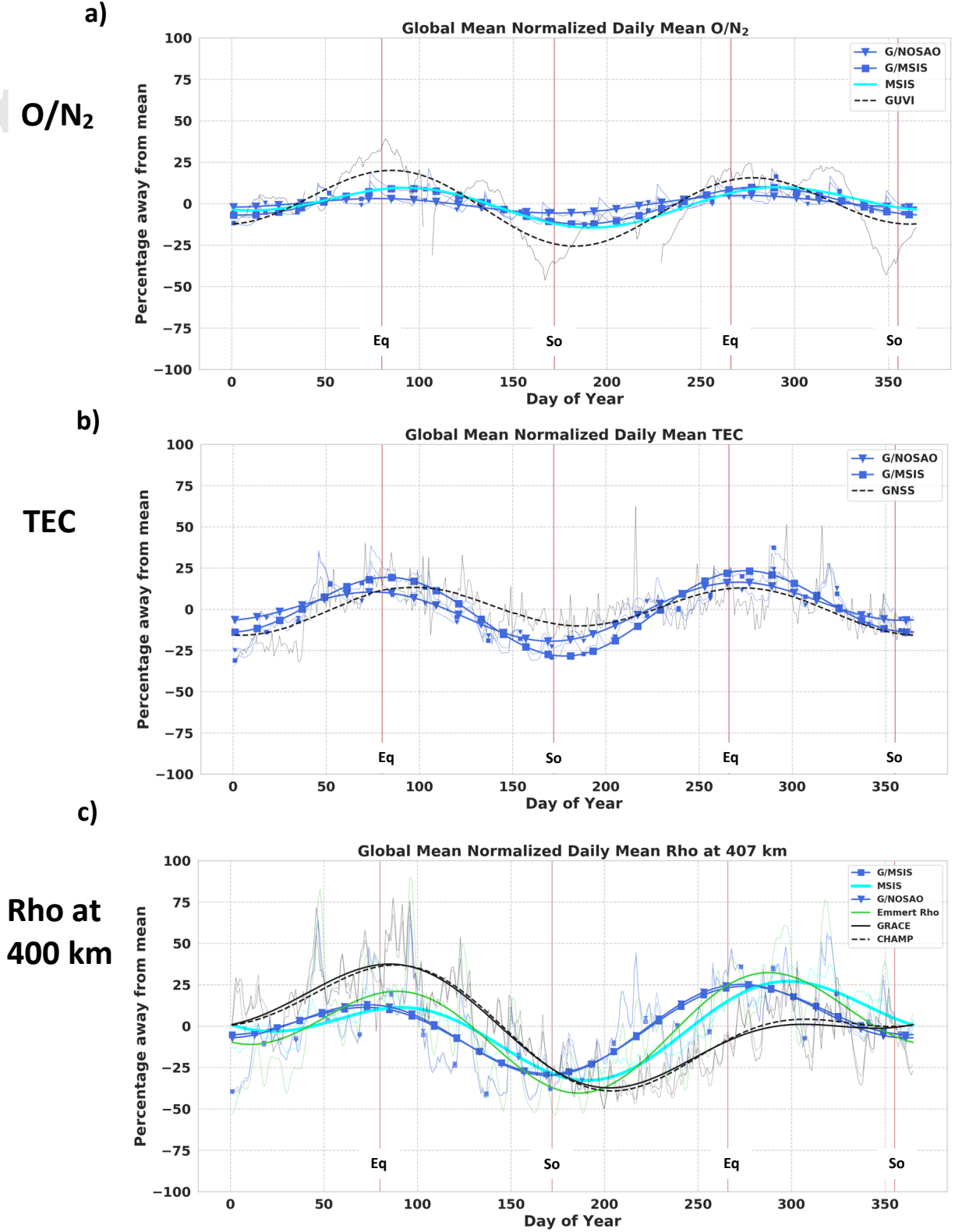


Figure 1. Diurnally Averaged Normalized a) O/N_2 , b) TEC, c) ρ at 400 km, for GITM simulations, MSIS and observational datasets. CHAMP and GRACE datasets are normalized to 400 km and averaged for 2007-2010 because of data gaps in 2010. The thin lines indicate the raw data and the thicker lines indicate the fitted values. The red vertical lines indicate the days of equinoxes (day 80 and day 266) and solstices (day 172 and 355).

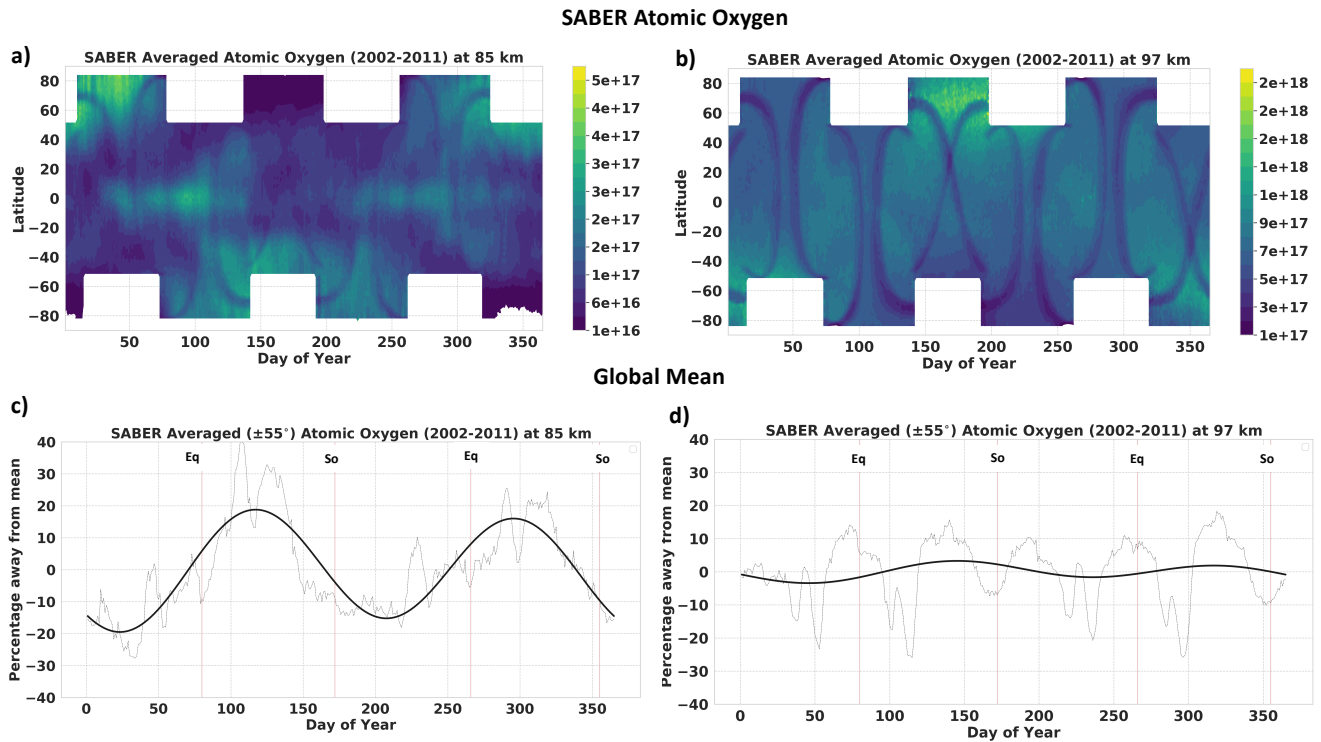


Figure 2. $[\text{O}]$ for SABER in m^{-3} , averaged for 2002-2011, binned by day of the year and latitude a) at 85 km, b) at 97 km. Area-weighted normalized global means spanning $\pm 55^\circ$ c) at 85 km, d) 97 km.

Author Manuscript

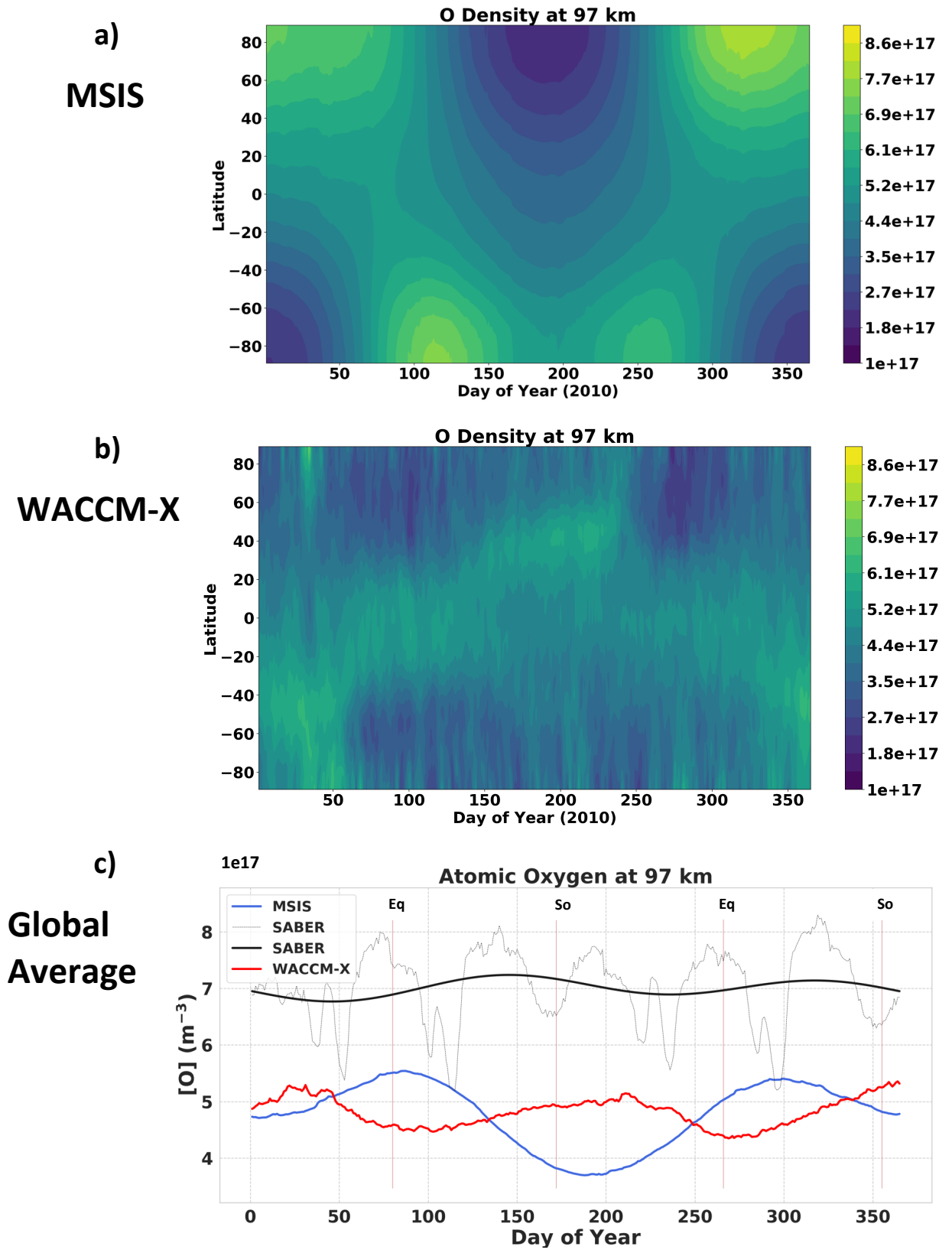


Figure 3. Diurnally averaged $[O]$ in m^{-3} for 2010 for a) MSIS, b) WACCM-X at 97 km. c) Area-weighted globally and diurnally averaged $[O]$ at 97 km. For SABER, the thin black line indicates the raw data and the thicker black line indicates the fitted values. SABER data is similar to that of Figure 2 and thus is the long-term average for 2002-2011. This article is protected by copyright. All rights reserved.

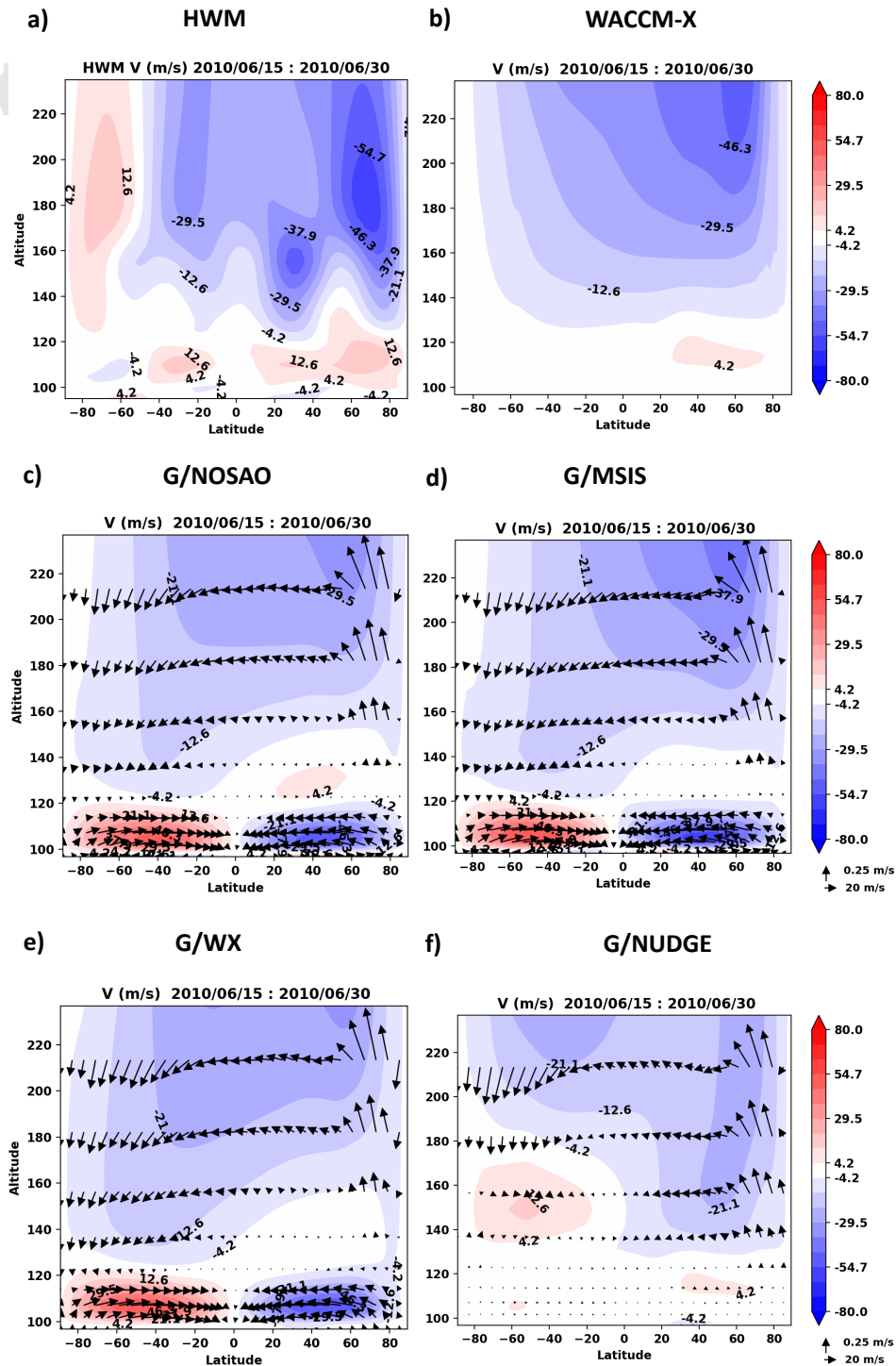


Figure 4. Latitude-Altitude cross-section of zonally and diurnally averaged meridional winds in m/s for 2010/06/15 - 2010/06/30 for a) HWM, b) WACCM-X, c) G/NOSAO, d) G/MSIS, e) G/WX, f) G/NUDGE. The negative values depict southward winds. Vectors indicate a sum of meridional and vertical winds (scaled by $\times 50$).

Author Manuscript

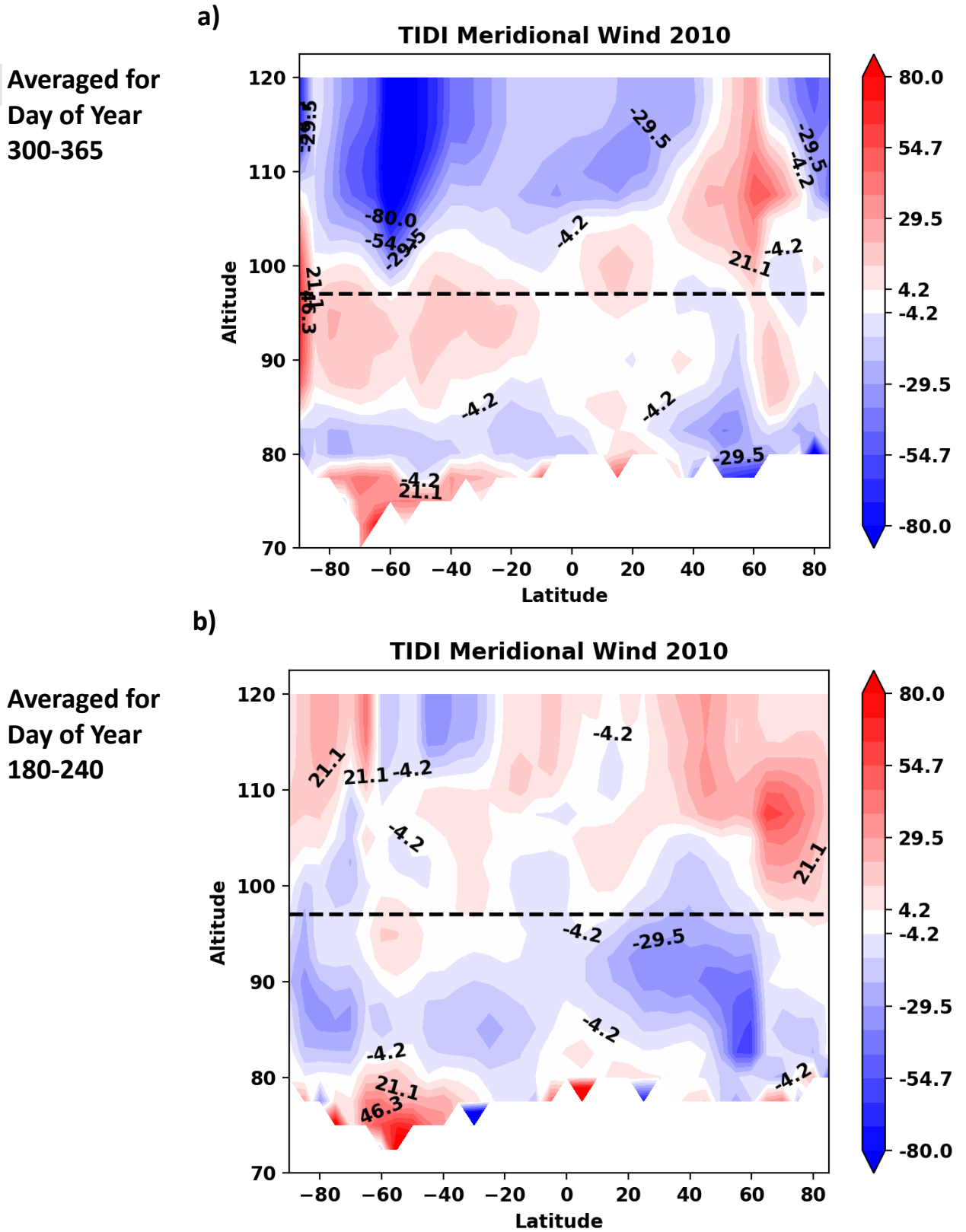


Figure 5. Averaged meridional winds in m/s for TIDI binned by latitude and altitude for days of the year a) 300-365 b) 180-240 in 2010. The dashed black horizontal line indicates the altitude of lower boundary of GITM, ~ 97 km.
 This article is protected by copyright. All rights reserved.

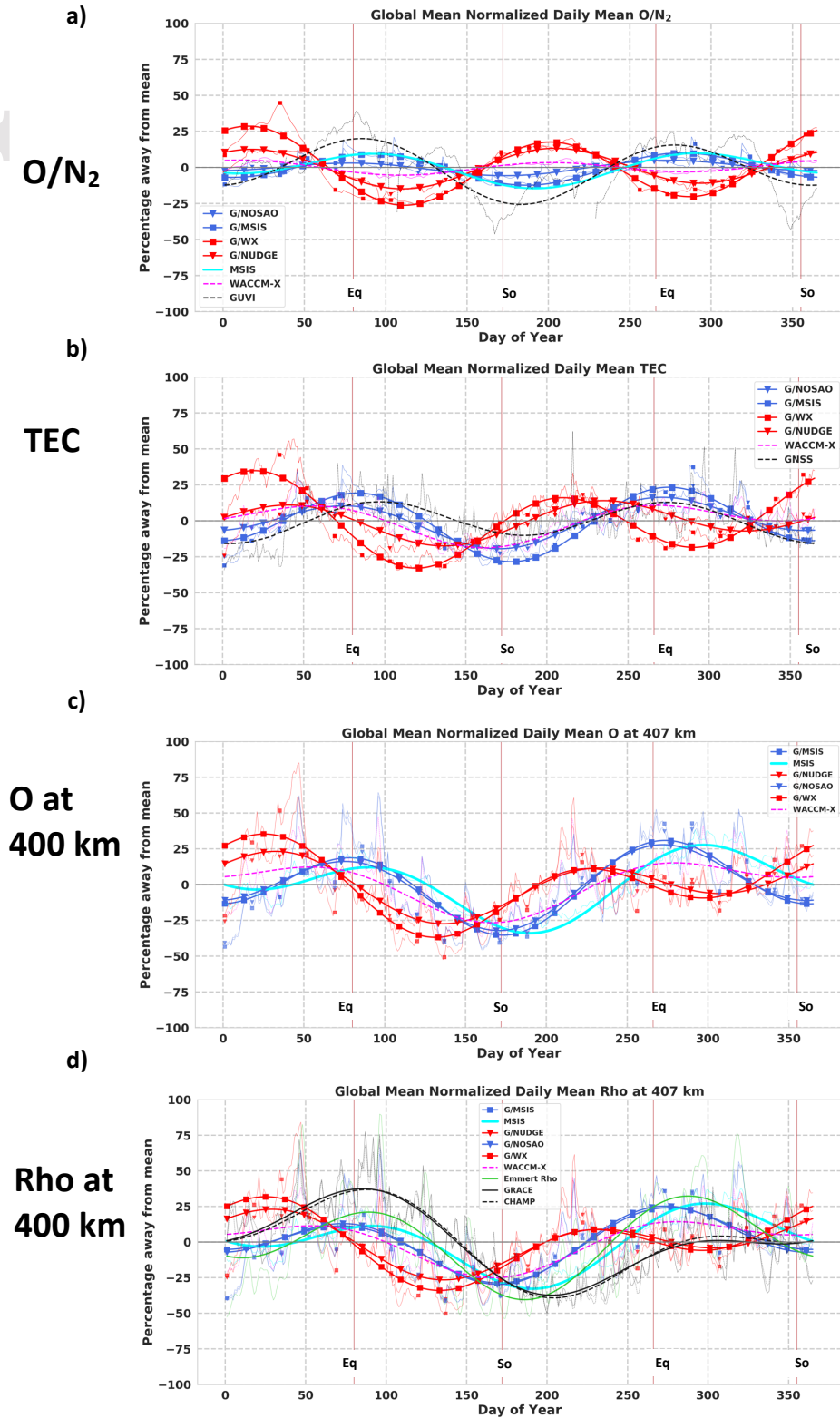
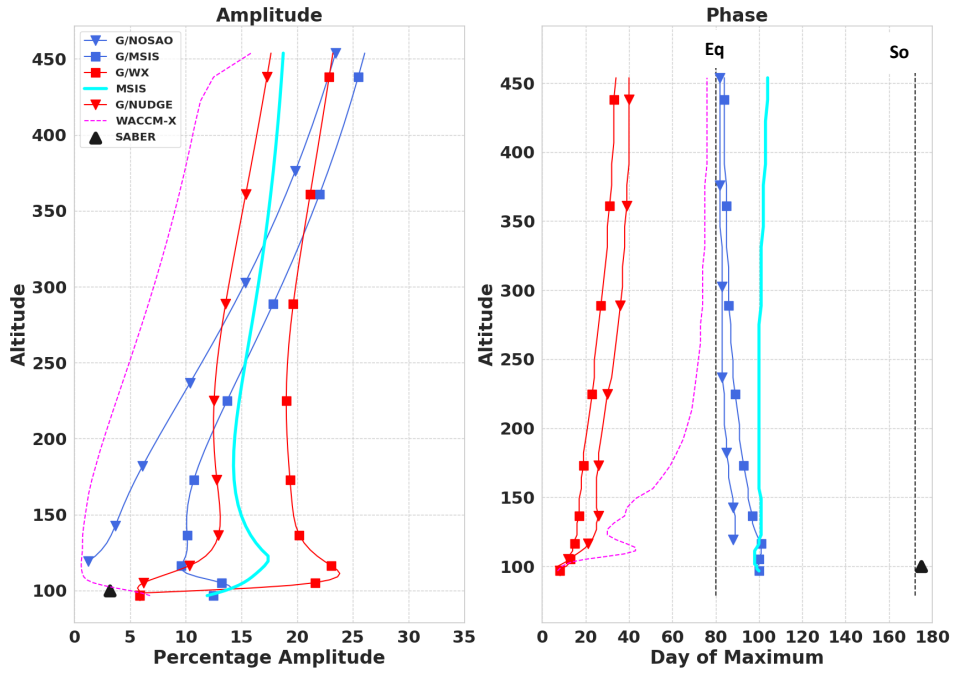


Figure 6. Diurnally averaged, normalized (area-weighted) global means a) O/N_2 , b) TEC, c) $[O]$ at 407 km, d) ρ at 407 km, for different GITM simulations, WACCM-X model, MSIS, and observational datasets. The thin lines indicate the raw data and the thicker lines indicate the fitted values. Similar to Figure 1, CHAMP and GRACE datasets are normalized to 400 km and averaged for 2007-2010. The red vertical lines indicate the days of equinoxes and solstices. The

This article is protected by copyright. All rights reserved.

a) Atomic Oxygen, O



b) Neutral Density, Rho

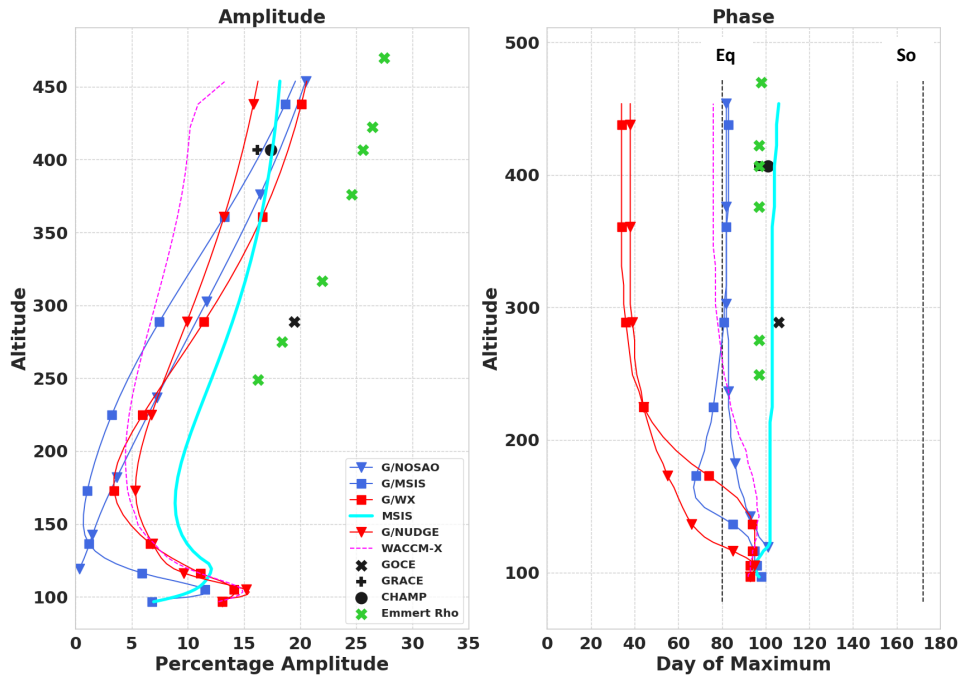


Figure 7. SAO Amplitudes and phases with altitude for a) [O] b) ρ , for different GITM simulations, WACCM-X model, MSIS, and observational datasets. SAO Amplitudes and phases are calculated from least squares fits to normalized daily averages of Figure 6. The phase signifies the day of first maximum. The vertical dashed black lines indicate the day of equinox (March 21) and solstice (June 21).

Author Manuscript

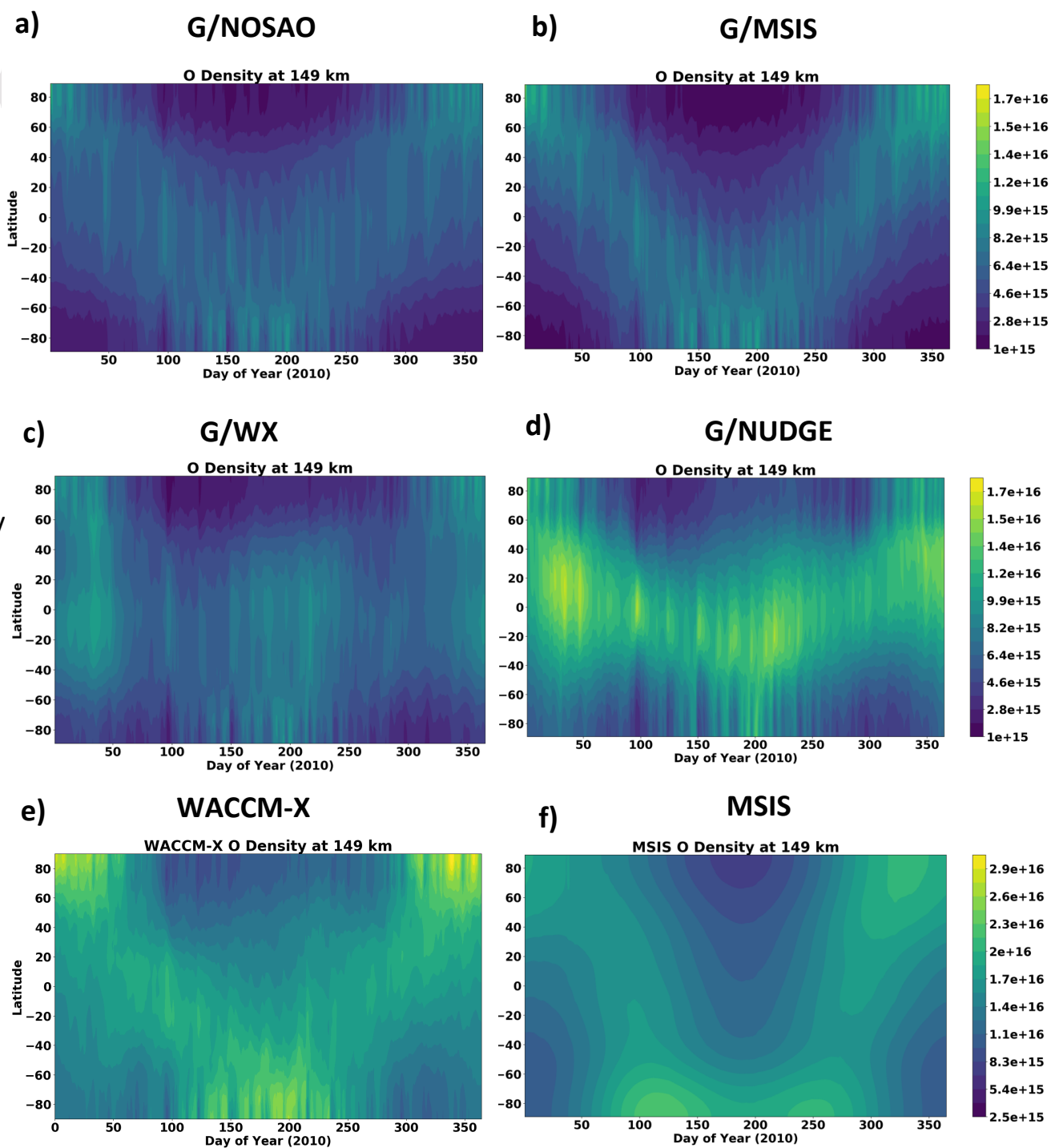


Figure 8. Diurnally averaged distribution of [O] with latitude in m^{-3} at 149 km for 2010 for a) G/NOSAO, b) G/MSIS, c) G/WX, d) G/NUDGE, e) WACCM-X, f) MSIS empirical model. This article is protected by copyright. All rights reserved.

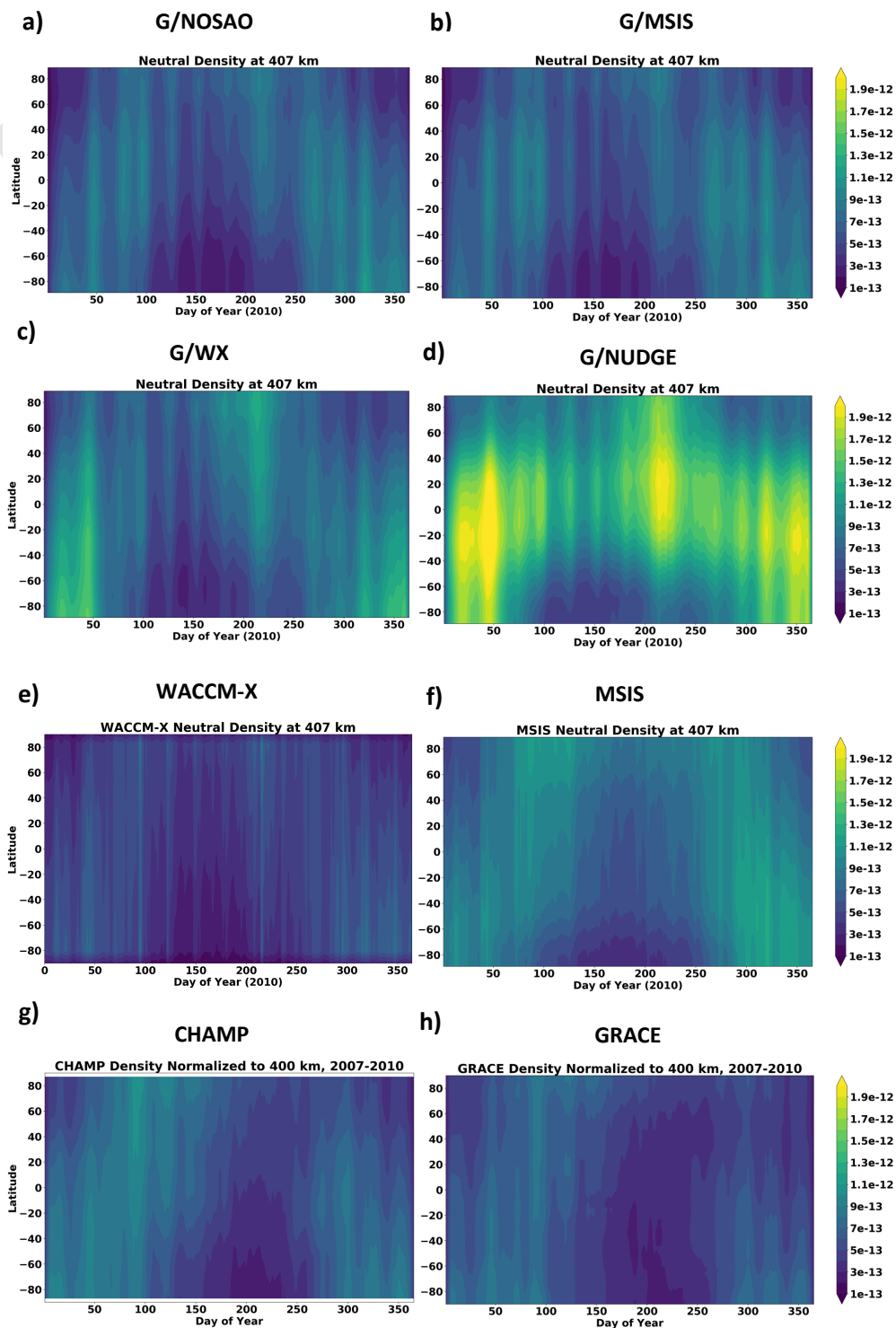


Figure 9. Diurnally averaged distribution of ρ with latitude in m^{-3} at 400 km for a) G/NOSAO, b) G/MSIS, c) G/WX, d) G/NUDGE, e) WACCM-X, f) MSIS empirical model, g) CHAMP, h) GRACE. CHAMP and GRACE datasets are normalized to 400 km and averaged from 2007-2010.

Author Manuscript

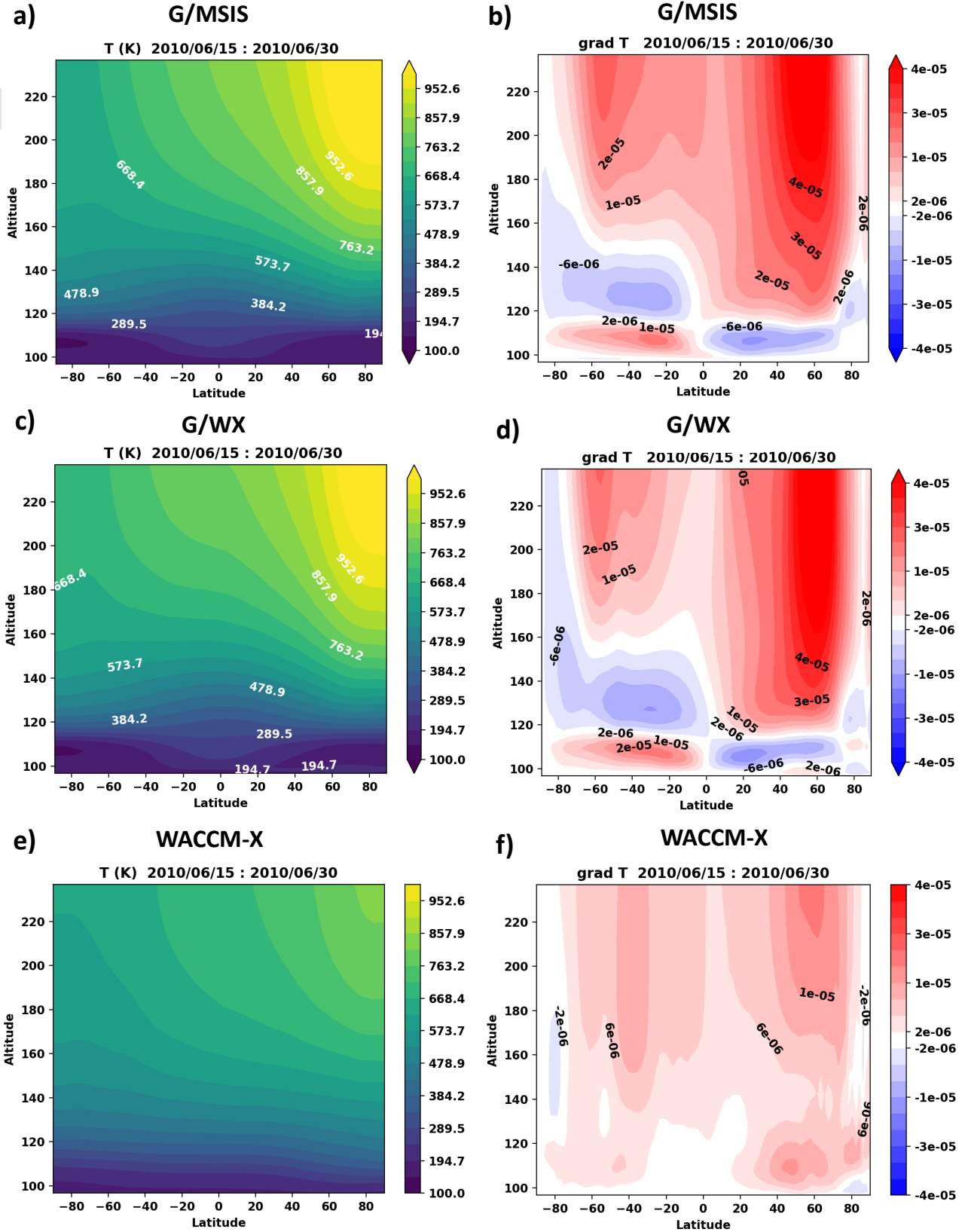


Figure 10. Latitude-Altitude cross-section of zonally and diurnally averaged Temperature in K for 2010/06/15 - 2010/06/30 for a) G/MSIS, c) G/WX, e) WACCM-X. Gradient in Temperature for each corresponding simulation is shown in the panel on the right. A positive gradient indicates that the temperature is larger towards the north.

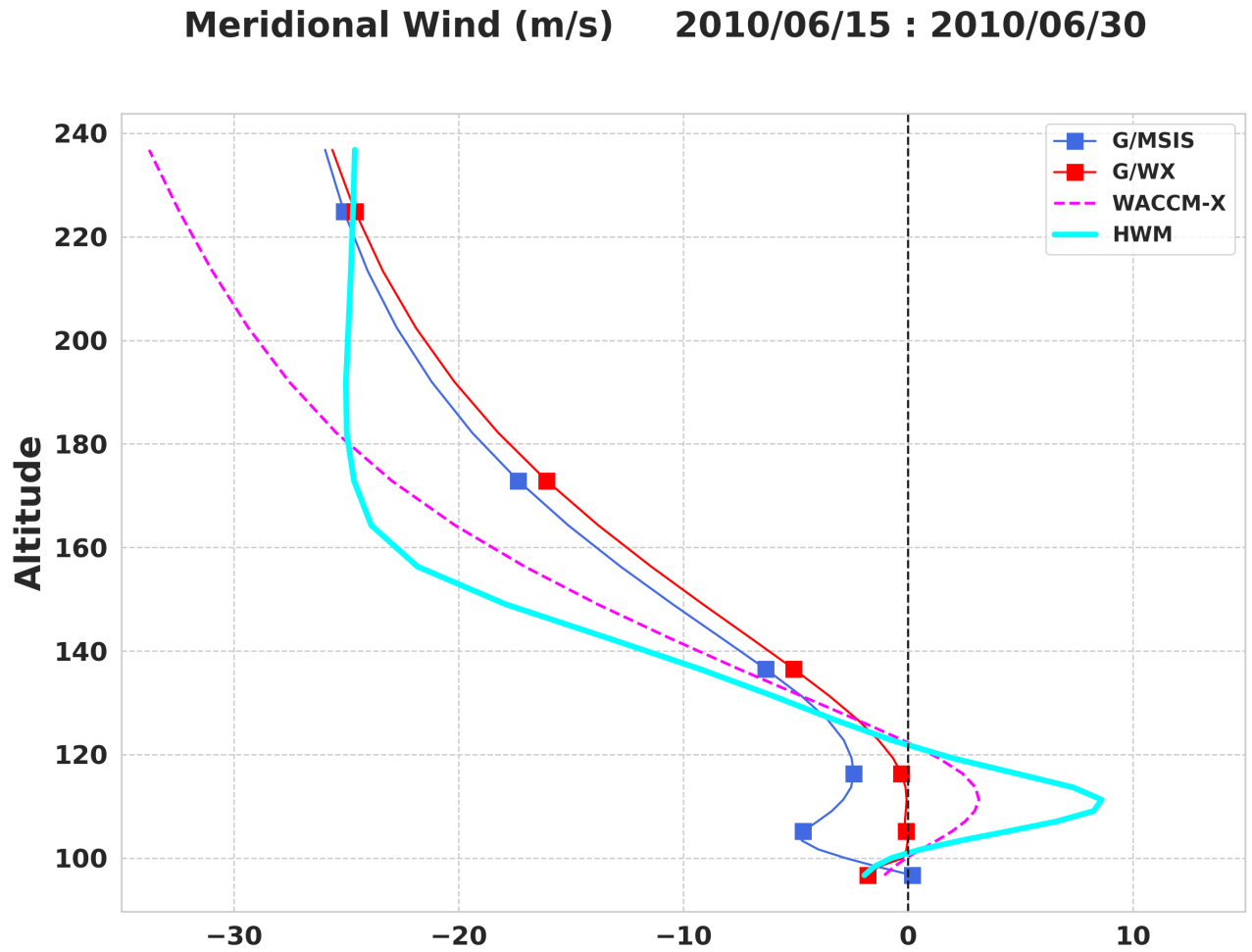


Figure 11. Globally averaged meridional winds in m/s for different GITM simulations, WACCM-X and HWM.

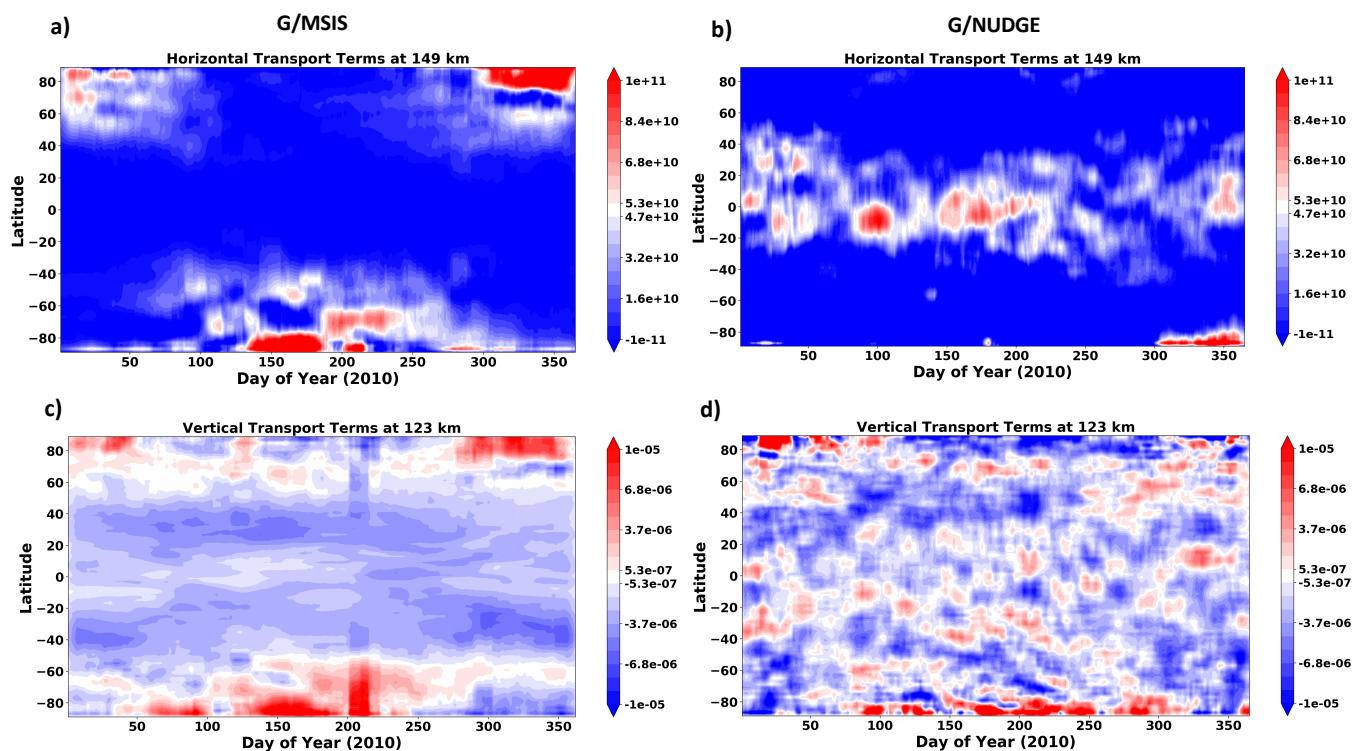


Figure 12. Diurnally averaged (15 day rolling mean) zonal means of transport terms. The panels on the left (right) are for G/MSIS (G/NUDGE). The top (bottom) panels are the horizontal (vertical) transport terms at 149 (123) km. Vertical transport terms have the units of s^{-1} and the horizontal transport terms have the units of $m^{-3}s^{-1}$.